Interplay between the plasma membrane and cell-cell adhesion maintains epithelial identity for correct polarised cell divisions

Manal M. Hosawi[1,2], Jiaoqi Cheng[1,2], Maria Fankhaenel[1,2], Marcin R. Przewloka[1,2,*] and Salah Elias[1,2,*,‡]

[1]School of Biological Sciences, University of Southampton, Southampton, SO17 1BJ, UK
[2]Institute for Life Sciences, University of Southampton, Southampton, SO17 1BJ, UK

[*]Correspondence: s.k.elias@soton.ac.uk; marcin.przewloka@soton.ac.uk
[‡]Lead Author

ABSTRACT

Polarised epithelial cell divisions represent a fundamental mechanism for tissue maintenance and morphogenesis. Morphological and mechanical changes in the plasma membrane influence the organisation and crosstalk of microtubules and actin at the cell cortex, thereby regulating the mitotic spindle machinery and chromosome segregation. Yet, the precise mechanisms linking plasma membrane remodelling to cell polarity and cortical cytoskeleton dynamics to ensure accurate execution of mitosis in mammalian epithelial cells remain poorly understood. Here we experimentally manipulated the density of mammary epithelial cells in culture, which led to several mitotic defects. Perturbation of cell-cell adhesion formation impairs the dynamics of the plasma membrane, affecting the shape and size of mitotic cells and resulting in defects in mitosis progression and generating daughter cells with aberrant architecture. In these conditions, F-actin-astral microtubule crosstalk is impaired, leading to mitotic spindle misassembly and misorientation, which in turn contributes to chromosome mis-segregation. Mechanistically, we identify the S100 Ca^{2+}-binding protein A11 (S100A11) as a key membrane-associated regulator that forms a complex with E-cadherin and the Leucine-Glycine-Asparagine repeat protein (LGN) to coordinate plasma membrane remodelling with E-cadherin-mediated cell adhesion and LGN-dependent mitotic spindle machinery. Thus, plasma membrane-mediated maintenance of mammalian epithelial cell identity is crucial for correct execution of polarised cell divisions, genome maintenance and safeguarding tissue integrity.

INTRODUCTION

Cell division requires equal partitioning of DNA into two daughter cells. To achieve this, each dividing cell builds a mitotic spindle that results from a spectacular rearrangement of microtubules

allowing proper alignment of chromosomes during metaphase and their equal separation during anaphase (Prosser and Pelletier, 2017). In polarised epithelia of multicellular organisms, the orientation of a correctly assembled mitotic spindle defines the position and fate of daughter cells, representing a fundamental mechanism that ensures the formation of structured and functional tissues (Lechler and Mapelli, 2021). Mitotic spindle orientation is regulated by an evolutionarily conserved ternary protein complex including the $G_{\alpha i}$ subunit of heterotrimeric G proteins, the Leucine-Glycine-Asparagine repeat protein (LGN) and the nuclear mitotic apparatus protein (NuMA) (di Pietro et al., 2016). During mitosis, the $G_{\alpha i}$-LGN-NuMA complex localises at the cell cortex, which facilitates the interaction of NuMA on astral microtubules and with the microtubule-associated minus-end motor Dynein, generating pulling forces on astral microtubules that ensure correct positioning of the mitotic spindle (Carminati et al., 2016; di Pietro et al., 2016; Okumura et al., 2018; Pirovano et al., 2019). Cumulative evidence shows that the crosstalk between astral microtubules and cortical F-actin is a key mechanism for balancing the cortical forces that ensure correct mitotic spindle and chromosome dynamics, as well as mitosis progression (di Pietro et al., 2017; Dogterom and Koenderink, 2019; Fankhaenel et al., 2023; Yu et al., 2019). In mammalian epithelia, junctional proteins including E-cadherin, Afadin, ABL1, SAPCD2 and Annexin A1 (ANXA1) have been shown to act as molecular landmarks instructing the polarised patterning of LGN and NuMA at the cell cortex to regulate the balance between planar and perpendicular mitotic spindle orientation (Carminati et al., 2016; Chiu et al., 2016; Fankhaenel et al., 2023; Gloerich et al., 2017; Matsumura et al., 2012). Yet, the mechanisms coordinating polarity cues with the cell cortex and the mitotic machinery in mammalian epithelial cells remain largely unknown.

During mitosis, cells transduce external cues to reorganise F-actin and microtubules at the cell cortex to control cell shape and balance intracellular tensions, thereby creating an optimal space for mitotic spindle formation and facilitate the subsequent correct alignment of the metaphase chromosomes (Lancaster et al., 2013; Leguay et al., 2022; Matthews et al., 2012; Matthews et al., 2020; Rizzelli et al., 2020; Serres et al., 2020; Taubenberger et al., 2020). While most of our knowledge of the mechanics of mitosis in mammalian cells comes from studies in non-polarised cells or cells grown in isolation on adhesive micropatterns (Ramkumar and Baum, 2016; Rizzelli et al., 2020; Taubenberger et al., 2020), increasing evidence shows that mitotic epithelial cells must maintain their native polarity and geometry to ensure correct mitotic spindle dynamics and chromosome segregation fidelity (Knouse et al., 2018; van Leen et al., 2020; Wang et al., 2018). Mitotic epithelial cells round up to push against tissue confinement ensuring cell mechanics that limits spindle assembly and chromosome segregation errors (Sorce et al., 2015), while sustaining adherens junctions with their neighbouring cells to maintain epithelial integrity (Baker and Garrod, 1993; Gloerich et al., 2017; Hart et al., 2017; Reinsch and Karsenti, 1994). Reciprocally, cell rounding is influenced by tensions and mechanical forces emanating from neighbouring cells, tissue topology as well as the growing and remodelling tissue itself (Rizzelli et al., 2020;

Taubenberger et al., 2020). Initial experiments in the amphibian eggs showed that the mitotic spindle aligns along the longest axis of the cell, following Hertwig's rule (Hertwig, 1884). Subsequent in-depth studies have shown that epithelial cell anisotropy determines mitotic spindle orientation, where moderately anisotropic cells follow partially Hertwig's rule, whereas elongated cells favour division along the major axis (van Leen et al., 2020). A few planar polarity cues such as Dishevelled and Vangl2 direct mitotic spindle orientation following Hertwig's rule (Box et al., 2019; Segalen et al., 2010). Further studies in the *Drosophila* pupal notum showed that LGN and NuMA localise to tricellular junctions to act as cell shape sensors and direct planar cell division along the major axis of the cell (Bosveld et al., 2016). Consistent with this, studies in the *Xenopus* epithelium reported that the mitotic spindle aligns to an axis of cell shape defined by the position of tricellular junctions, which requires functional cell-cell adhesion E-cadherin protein and the localization of LGN to tricellular junctions (Nestor-Bergmann et al., 2019). However, studies in *canine* kidney MDCK cells showed that E-cadherin and cortical LGN align epithelial cell divisions with tissue tension independently of cell shape, and that the localisation of E-cadherin at the plasma membrane is key to pattern LGN at the cell cortex (Gloerich et al., 2017; Hart et al., 2017). The precise molecular mechanisms allowing E-cadherin-mediated adhesion to transduce external cues to ensure correct execution of polarised cell divisions remains not well understood in mammalian epithelial cells.

Mitotic cells undergo dynamic changes in their volume and surface topology, driven by remodelling in the plasma membrane, which responds to mechanical stresses and connects with the cortex to fine-tune intracellular tensions that control the orientation, progression, and outcome of cell division (Carlton et al., 2020; Ramkumar and Baum, 2016). Depletion of plasma membrane proteins such as the G protein-coupled receptors can inhibit cell division (Zhang et al., 2012; Zhang and Eggert, 2013). Other studies reported differences in the cell surface proteome between interphase and metaphase cells (Ozlu et al., 2015). In single HeLa cells, elongation of the plasma membrane is coordinated with cortical localisation of Dynein to centre the mitotic spindle in anaphase and achieve symmetric cell division (Kiyomitsu and Cheeseman, 2013). In these cells, polar plasma membrane blebbing, stabilises cell shape by relieving actomyosin cortical tensions ensuring the stability of cleavage furrow positioning for correct progression of cytokinesis (Sedzinski et al., 2011). In polarised epithelial cells, on the other hand, decrease in intracellular tensions relies on traction forces from neighbouring cells in addition to those emanating from the extracellular matrix (Uroz et al., 2019; Uroz et al., 2018), further highlighting the functional requirement of cell-cell signalling for correct execution of polarised cell divisions. However, it remains unknown how mitosis dynamic progression and outcome are coordinated with plasma membrane remodelling and cell-cell adhesion.

Here we exploit a simple monolayer culture system combined with fluorescence time-lapse and confocal imaging to experimentally manipulate the density of mammary epithelial cells and examine how perturbation of cell-cell adhesion formation influences the orientation, mechanics,

and outcome of cell division. We show that cells grown at low density lose their polarised epithelial identity and display aberrant dynamics of the plasma membrane during mitosis, which affects the size and shape of mitotic cells resulting in daughter cells with architectural defects. In these non-polarised conditions, cortical actin organisation and its interaction with astral microtubules are impaired. Consequently, cells fail to correctly align the mitotic spindle and chromosomes, leading to delayed mitosis progression and cytokinesis defects. In this experimental context, we investigated the function of the membrane associated protein S100A11 (S100 Ca^{2+}-binding protein A11), which we identified recently in a proteomic screening of mitotic mammary epithelial cells (Fankhaenel et al., 2023). S100A11 associates to the plasma membrane in a Ca^{2+}-dependent manner and has been shown to regulate plasma membrane repair in migrating cells, by facilitating F-actin dynamic organisation and plasma membrane remodelling (Jaiswal et al., 2014; Mohammed et al., 2023). S100A11 is enriched in pseudopodia of metastatic cancer cells and is required for the formation of actin-dependent pseudopodia protrusions and tumour cell migration (Shankar et al., 2010). Furthermore, S100A11 has been identified as an interactor of E-cadherin at adherens junctions (Guo et al., 2014). In mitotic mammary epithelial cells, we recently showed that localisation of S100A11 and its direct partner ANXA1 to the plasma membrane is required for polarised accumulation of LGN at the lateral cortex to promote planar cell division (Fankhaenel et al., 2023). However, the precise function of S100A11 in mitosis has not been characterised yet. In the present experiments, we demonstrate that S100A11 is required for proper plasma membrane remodelling to ensure faithful segregation of chromosomes and the generation of equal-sized daughter cells. We show that S100A11 forms a complex with E-cadherin and LGN to instruct correct E-cadherin-mediated adhesion and lateral patterning of the LGN spindle orientation machinery, thereby ensuring planar cell division. S100A11 depletion phenocopies the mitotic defects observed in non-polarised cells and alters epithelial integrity. Collectively, the present experiments shed new light onto the importance of epithelial identity maintenance for correct dynamics, mechanics, and outcome of polarised cell divisions, and suggest S100A11-mediated plasma membrane remodelling as a mechanism coordinating the mechanochemical crosstalk between cell-cell adhesion, the cell cortex and mitotic spindle machinery in mammary epithelial cells.

RESULTS

Epithelial cell density-dependent plasma membrane remodelling influences mitosis progression and outcome

To examine the functional requirement of cell-cell adhesion for correct plasma membrane remodelling during cell division, we used human MCF-10A mammary epithelial cells cultured at optimal or low density (**Figure 1A**). Characterisation of MCF-10A monolayers 72 hours (h) after plating reveals that cells cultured at optimal density establish E-cadherin adherens junctions,

whereas cells cultured at low density lose their polarised epithelial identity and fail to form correct cell-cell adhesions with E-cadherin abnormally accumulating in the cytoplasm both in interphase and metaphase, allowing us to define optimal-density MCF-10A cells as polarised, and low-density MCF-10A cells as non-polarised (**Figures 1A and 1B**). Next, we performed live imaging in polarised and non-polarised MCF-10A cells, in which we labelled the plasma membrane with CellMask^{TM} and DNA with Hoechst 33342. Consistent with previous studies (Chaigne et al., 2021), CellMask^{TM} displays a homogeneous, circumferential distribution at the cell surface of polarised mitotic cells, which generate equal-sized daughter cells at cytokinesis (**Figures 1C-1E; Movie S1**). In non-polarised mitotic cells, however, the plasma membrane has aberrant dynamics with ~52% and ~39% of cells displaying a unilateral and bilateral accumulation of CellMask^{TM} at the cell surface, respectively (**Figures 1C-1E; Movie S2; Movie S3**). Perturbation of cell-cell adhesion formation affects the size and shape of non-polarised cells which display a mesenchymal behaviour associated with polar, asymmetric elongation of the plasma membrane during anaphase in ~77% of mitotic cells (**Figures 1C and 1F**). In these conditions, sister chromatids are off-centred from anaphase until telophase, which affects the position of the cleavage furrow and generates unequal-sized daughter cells at cytokinesis in ~44% of non-polarised mitotic cells (**Figures 1G and 1H**), consistent with previous findings in HeLa cells (Kiyomitsu and Cheeseman, 2013). During anaphase-to-telophase transition, the plasma membrane of non-polarised cells forms blebs in the polar area opposing the expanding cell cortex but this fails to re-centre the sister chromatids or stabilise the cleavage furrow (**Figure 1C and 1I**), which disagrees with previous studies showing that polar membrane blebbing influences the position and stability of the mitotic spindle and cleavage furrow (Kiyomitsu and Cheeseman, 2013; Sedzinski et al., 2011). Interestingly, a close examination of the CellMask^{TM} labelling in non-polarised cells reveals an accumulation of cytoplasmic vesicles, some of which localise to the cleavage furrow (**Figure 1C**). Thus, asymmetric membrane elongation may involve both remodelling and *de novo* incorporation of membrane components into the cleavage furrow. We also observed significant defects in the dynamics of cell division in a vast majority of non-polarised cells as compared to polarised cells, with the proportion of cells that completed mitosis decreasing significantly in low-density cell cultures (non-polarised: ~50% versus polarised: ~94%) (**Figure 1J**). In non-polarised cells that completed their division, the duration of mitosis is extended (**Figure 1C**), as revealed by increased average transition time from nuclear envelope breakdown (NEBD) to cytokinesis (non-polarised: ~98 min versus polarised: ~62 min) (**Figure 1K**), consistent with a recent study in MDCK cells showing that epithelial density influences progression of the cell cycle (Donker et al., 2022). Together, these data suggest that cell-cell adhesion and plasma membrane remodelling are coordinated to maintain polarised epithelial identity, thereby ensuring correct mitosis mechanics and progression as well as symmetric cytokinesis.

Epithelial cell density-dependent mitotic spindle dynamics and chromosome segregation fidelity

The results above strongly suggest that epithelial cell density influences the assembly and alignment of the mitotic spindle, which in turn ensures correct chromosome dynamics and segregation. To test this hypothesis, we performed live imaging of polarised and non-polarised MCF-10A cells, in which we labelled microtubules with SiR-tubulin (Lukinavicius et al., 2014) and DNA with Hoechst 33342 (**Figure 2A**). We identified several mitotic defects in non-polarised cells (**Figures 2A and 2B; Movie S4; Movie S5; Movie S6; Movie S7**). We observed significant defects in chromosome alignment and segregation in ~60% and ~27% of non-polarised cells, respectively, leading to a significant increase in the proportion of daughter cells inheriting micronuclei at cytokinesis (non-polarised: ~15 % versus polarised: 0%) (**Figures 2A and 2B, Movie S5**). The morphology of the mitotic spindle is also affected, with ~35% of non-polarised cells displaying abnormal bipolar spindles (**Figures 2A and 2B; Movie S7**). During metaphase, polarised cells align their mitotic spindle parallel to the substratum plane (~4°), whereas non-polarised cells display spindle orientation defects (~10°), which persist during anaphase (non-polarised: ~9° versus polarised: ~4°) (**Figure 2C**). We further confirmed these observations using immunofluorescence and confocal imaging (**Figure 2D**). Our live imaging experiments also show that ~93% of non-polarised cells display excessive oscillations of the mitotic spindle relative to the *z* axis between successive time frames during metaphase, whereas in polarised cells the spindle does not display notable oscillatory *z* rotations and remains in a planar position (**Figures 2E-2G**). There is also an increase in the oscillatory rotations of the mitotic spindle in the *xy* plane in non-polarised cells as compared to polarised cells, but the difference is not significant (**Figures 2H-2J**). Nonetheless, while all investigated polarised cells align their mitotic spindle following Hertwig's rule in the *xy* plane, only ~28% of non-polarised cells follow this rule (**Figures S1A and S1B**). Thus, cell-cell adhesion-mediated polarisation of mammary epithelial cells ensures correct mitotic spindle assembly and dynamic orientation, and in turn faithful chromosome segregation.

Epithelial cell density-dependent re-organisation of cortical actin during mitosis

Dynamic re-organisation of actin cytoskeleton into a uniform, contractile cortex at the cell surface at mitotic entry ensures proper assembly and orientation of the mitotic spindle by polarising cortical force-generating proteins that pulls on astral microtubules (Carminati et al., 2016; Fankhaenel et al., 2023; Yu et al., 2019). This cortical actin network is important for accurate control of cell rounding, which peaks during metaphase (Rizzelli et al., 2020; Taubenberger et al., 2020). In epithelial cells, mitotic rounding defects result in abnormal spindle assembly and orientation, division asymmetries as well as delayed mitosis progression (Chanet et al., 2017; Lancaster et al., 2013). To investigate how perturbation of cell-cell adhesion formation influences cortical actin re-organisation during mitosis, we performed live imaging in MCF-10A cells stably expressing Lifeact-mCherry and labelled with SiR-tubulin (**Figure 3A; Movie S8; Movie S9**). We

measured cortical thickness in metaphase, which is a key readout of cortical actin architecture (Serres et al., 2020), and found that perturbation of cell-cell adhesion formation leads to an increase in cortex thickness (**Figure 3B**). F-actin fluorescence intensity also increases in both the cortical and subcortical regions of non-polarised metaphase cells (**Figure 3C**). Consequently, non-polarised cells are rounder, and the rounding-up process is faster as compared to polarised cells (non-polarised: ~20 min versus polarised: ~28 min) (**Figures 3D and 3E**). We confirmed these observations by immunofluorescence and confocal imaging, which also reveal a decrease in the depth of the subcortical actin cloud in non-polarised cells (non-polarised: ~5 μm versus polarised: ~8 μm) (**Figures 3F and 3G; Figures S2A-S2C**). The subcortical actin cloud has been shown to mediate cortical forces and to concentrate force-generating proteins at the retraction fibres acting on centrosome dynamics and pulling on astral microtubules to orient the mitotic spindle (Kwon et al., 2015). We show that subcortical actin cloud thinning is associated with impaired astral microtubule length in non-polarised cells (non-polarised: ~19 nm versus polarised: ~16 nm) while their relative intensity remains unaffected, suggesting their stabilisation (**Figures 3H and 3I**). Finally, the length of the mitotic spindle as well as the fluorescence intensity of spindle microtubules increase in non-polarised cells as compared to polarised cells (**Figures S2D and S2E**). Thus, cell-cell adhesion-mediated polarised epithelial cell identity defines the dynamic re-organisation of the actin cortex and its interaction with astral microtubules to ensure correct mitotic spindle dynamics and mitotic cell rounding.

S100A11 coordinates plasma membrane remodelling with cell-cell adhesion and cortical cytoskeleton organisation during mitosis

We recently characterised the LGN cortical interactome in mitotic mammary epithelial cells, where we identified ANXA1 as a polarity cue that controls planar mitotic spindle orientation (Fankhaenel et al., 2023). Our proteomic screening also identified S100A11, an established partner of ANXA1 (Rintala-Dempsey et al., 2008), but which the function in mitosis has not been characterised previously. Our recent findings along with previous studies showing that S100A11 is required for plasma membrane remodelling by mediating a dynamic interplay between the plasma membrane and F-actin (Jaiswal et al., 2014; Mohammed et al., 2023), and the fact S100A11 interacts with E-cadherin (Guo et al., 2014), prompted us to test whether S100A11 function in the regulation of plasma membrane remodelling may influence cell-cell adhesion integrity and F-actin re-organisation during mitosis. Using immunofluorescence and confocal imaging, we conducted a first characterisation of the localisation of S100A11 during the cell cycle and revealed that S100A11 distributes in the cytoplasm and accumulates at the plasma membrane of mitotic polarised MCF-10A cells (**Figure 4A**). Plasma membrane localisation of S100A11 is impaired in non-polarised cells (**Figures 4A and 4B**). To examine the role of S100A11 in plasma membrane remodelling during mitosis, we performed live imaging in control and S100A11-depleted MCF-10A cells grown at optimal density, which we labelled with CellMask™ (**Figure 4C; Movie S10; Movie**

S11). We observed unequal distribution of CellMask^{TM} in a vast majority of S100A11-depleted cells (si-S100A11#1: ~79% versus si-Control: ~26%), which display a mesenchymal behaviour and asymmetric plasma membrane elongation during mitosis (**Figures 4C and 4D**), like our observations in cells grown at low density. The proportion of cells that completed mitosis decreases significantly upon S100A11 knockdown (si-S100A11#1: ~61% versus si-Control: ~98%) (**Figure 4E**). S100A11-depleted cells that completed mitosis display chromosome alignment and segregation defects in ~16% and ~67% of cells, respectively (**Figure 4F**). Immunofluorescence and confocal imaging reveal that S100A11 knockdown impairs the localisation of E-cadherin at adherens junctions at 48 h post-S100A11 knockdown, while the total cellular levels of E-cadherin do not change (**Figures 4G and 4H**). These defects in cell-cell adhesion persist at 72 h post-S100A11 depletion (**Figure S3**). A close examination of the localisation of E-cadherin in metaphase cells shows that the protein accumulates in the cytoplasm and fails to cluster properly at adherens junctions of S100A11-depleted cells (**Figures 4I and 4J**). This impairs cell-cell adhesion integrity and results in significant defects in the cytoarchitecture of S100A11-depleted cells (**Figures 4K and 4L**). Consistent with this, S100A11 knockdown abrogates the assembly of single tight F-actin bundles at cell-cell contacts (**Figures 5A-5C**). Actin bundles ensure structural support of the plasma membrane (Zsolnay et al., 2020) and function as mechanosensors maintaining epithelial cell mechanics and integrity (Narayanan et al., 2015; Ruckerl et al., 2017). S100A11 knockdown also impairs the organisation of cortical F-actin and its interaction with astral microtubules during metaphase, of which the length is also affected (**Figures 5D-5F**). Our results indicate that S100A11 is a key membrane-associated protein that coordinates plasma membrane remodelling with cell-cell adhesion maintenance and cell cortex organisation during mitosis.

S100A11 forms a complex with E-cadherin and LGN to control mitotic spindle orientation

Direct binding of LGN to E-cadherin and its Afadin-mediated interaction with cortical F-actin regulates the localisation and function of NuMA-Dynein-Dynactin to generate cortical forces that orient the mitotic spindle in epithelial cells (Carminati et al., 2016; Gloerich et al., 2017). Our results described above and previous findings of other labs showing that S100A11 interacts with E-cadherin (Guo et al., 2014) and F-actin (Shankar et al., 2010), prompted us to test whether S100A11 regulates LGN-mediated mitotic spindle orientation. First, we performed affinity purification to isolate the S100A11 complex from stable MCF-10A cells expressing GFP-S100A11 and arrested in metaphase (**Figure 6A**). GFP-S100A11 distributes in the cytoplasm and localises to the cell surface throughout the cell cycle (**Figure S4A**; **Movie S12**), consistent with recent studies in HeLa and U2OS osteosarcoma cells (Mohammed et al., 2023). We validated synchronisation efficiency by accessing the accumulation of phospho-Histone H3 (**Figure S4B**). Our pull-down assays combined with western blotting analysis reveal that GFP-S100A11 co-precipitates LGN and E-cadherin (**Figure 6A**). Previously, endogenous S100A11 has been co-

purified in a reciprocal manner with GFP-LGN (Fankhaenel et al., 2023) and E-cadherin-BirA* (Guo et al., 2014). Furthermore, we reveal that endogenous S100A11 co-localises with E-cadherin to the cell surface in polarised epithelial cells, whereas the two proteins co-accumulate in the cytoplasm of non-polarised cells (**Figures 6B and 6C**). Next, we performed immunofluorescence and confocal imaging to evaluate the extent to which S100A11 affects the localisation of LGN at the lateral cortex during metaphase. S100A11 knockdown impairs the bilateral cortical distribution of LGN observed in control cells, with a significant increase in the proportion of S100A11-depleted cells displaying a unilateral accumulation of LGN (si-S100A11#1: ~45%; si-S100A11#2: ~52%; si-Control: ~11%) (**Figures 6D and 6E**). These results further suggest that S100A11 regulates mitotic spindle orientation. We tested this hypothesis directly by immunofluorescence and confocal imaging and found that S100A11 knockdown results in mitotic spindle misorientation, with spindle angles αz increasing from ~4° in controls to ~10° and ~14° in cells treated with si-S100A11#1 and si-S100A11#2, respectively (**Figures 6F and 6G**). Interestingly, E-cadherin knockdown impairs the recruitment of LGN to the cell cortex (**Figures 6H-6J**), but moderately affects S100A11 localisation at the plasma membrane (**Figures 6K and 6L**), suggesting that S100A11 may act upstream of E-cadherin to control the mitotic spindle orientation machinery.

DISCUSSION

Polarised cell divisions are crucial for mammalian epithelial tissue differentiation, integrity and function, by defining the fate and position of daughter cells (Lechler and Mapelli, 2021). Recent evidence has shown that epithelial polarity influences the orientation, progression, and outcome of cell division, including how chromosomes segregate to daughter cells (Gloerich et al., 2017; Hart et al., 2017; Knouse et al., 2018; Lechler and Mapelli, 2021; Wang et al., 2018). However, most of our mechanistic knowledge of how cell shape dictates the dynamic progression of mammalian cell divisions has advanced, largely from studies in non-polarised or isolated cells grown on adhesive micropatterns (Kiyomitsu and Cheeseman, 2013; Rizzelli et al., 2020; van Leen et al., 2020). While these studies have extensively described the influence of adhesive substrates and the extracellular matrix on the mechanics of mitosis by regulating the crosstalk between cortical cytoskeleton and the mitotic machinery (Rizzelli et al., 2020; Taubenberger et al., 2020), how these mechanisms are coordinated with plasma membrane signalling and cell-cell adhesion remains poorly defined. Our present experiments in mammary epithelial cells uncover a functional interplay between plasma membrane remodelling and cell-cell adhesion, which maintains epithelial cell identity for correct dynamics and outcome of polarised cell divisions. We further report that cell-cell adhesion assembly dictates plasma membrane remodelling and F-actin-astral microtubule crosstalk to control the shape and size of mitotic cells, which in turn ensures proper mitotic spindle dynamics and faithful chromosome segregation, as well as

symmetric separation of daughter cells during cytokinesis. At the molecular level, we identify S100A11 as an upstream membrane-associated cue that coordinates correct plasma membrane remodelling with cell-cell adhesion maintenance and cortical cytoskeleton re-organisation during mitosis. We demonstrate that S100A11 complexes with E-cadherin and LGN to direct their polarised localisation to the lateral cortex for correct orientation, progression, and outcome of mammary epithelial cell divisions (**Figure 7**). Together, our findings shed new light on the function of the plasma membrane as a molecular signalling platform coordinating cell adhesion-mediated mechanochemical crosstalk between mitotic epithelial cells and their tissue environment to maintain their epithelial identity and execute error-free cell divisions.

Most studies addressing the role of external cues in the regulation of mammalian cell divisions have been carried out in isolated cells grown on adhesive micropatterns, a method pioneered by Bornens and Théry (Thery et al., 2007). These studies have shown that mitotic focal/substrate adhesion, maintained by integrin signalling, is key for correct chromosome and mitotic spindle dynamics and cytokinesis (Dix et al., 2018; Knouse et al., 2018; Lechler and Fuchs, 2005; Taneja et al., 2016). Nonetheless, cell-cell adhesions are essential for epithelial cells to acquire a defined shape and polarity, which are maintained to ensure correct execution of the mitotic machinery (Ragkousi and Gibson, 2014; Ramkumar and Baum, 2016; Taubenberger et al., 2020). Disruption of tissue architecture in several mammalian epithelial tissues such as skin, liver, prostate, and mammary gland, affects cell shape and polarity leading to defects in chromosome segregation and mitotic dynamics (Knouse et al., 2018; Wang et al., 2018). Our experiments show that perturbation of cell-cell adhesion assembly in mammary epithelial cells cultured at low density abrogates E-cadherin localisation to the cell surface, which affects cell shape throughout mitosis. Our results suggest, but do not prove, that perturbation of cell-cell adhesion affects plasma membrane remodelling, which elongates asymmetrically to generate unequal-sized daughter cells at cytokinesis. This is in sharp contrast with studies in isolated HeLa cells, showing that Anillin-RANGTP-dependent plasma membrane asymmetric elongation corrects mitotic spindle positioning defects during late anaphase and ensure symmetric cell division (Kiyomitsu and Cheeseman, 2013). Our observations that asymmetric elongation of the plasma membrane upon perturbation of cell-cell adhesion assembly results in mitotic spindle and sister chromatid mispositioning that persist until telophase, indicate that additional molecular mechanisms coordinate plasma membrane remodelling and mitotic spindle dynamics in polarised epithelial cells. Remodelling of the plasma membrane in HeLa cells is accompanied with polar cortical blebbing which re-centres the mitotic spindle and releases cortical tensions to stabilise cell shape and ensure correct positioning of the cleavage furrow (Kiyomitsu and Cheeseman, 2013; Sedzinski et al., 2011). Our results in non-polarised mammary epithelial cells showing that blebbing does not rescue defects in mitotic spindle, sister chromatids and cleavage furrow positioning, reinforce a model whereby E-cadherin-mediated cell-cell adhesion is crucial for mitotic cells to sense and integrate external forces from neighbouring cells, which in turn

decreases intercellular cortical tensions to ensure symmetric cell division. Thus, mammary epithelial cells must interact with their tissue environment to maintain their epithelial identity and native geometry to execute error-free mitosis. Importantly, one must be cautious when modelling and generalising some mechanisms of cell division; cellular identity (in this case, the epithelial origin) defines the response of mitotic cells to certain environmental cues, which may not be observed in non-epithelial cells.

We show that non-polarised mitotic mammary epithelial cells roundup faster and are rounder as compared to polarised cells, further pointing to differences with findings in isolated cells (Serres et al., 2020) and the important role of cell-cell adhesion in the regulation of the mechanics of mitosis in epithelial cells. Re-organisation of the actomyosin cytoskeleton into a uniform, contractile cortical meshwork, is a key mechanism for the generation of cortical tensions at the cell surface that drive mitotic rounding, which culminates during metaphase (Rizzelli et al., 2020; Taubenberger et al., 2020). Remarkably, we found that perturbation of cell-cell adhesion assembly leads to an increase in the thickness of cortical F-actin in metaphase cells, which correlates with efficient rounding. This contrasts with findings in isolated HeLa cells where the thinning of cortical actin is crucial for generating cortical tensions that drive efficient mitotic rounding (Serres et al., 2020). We speculate that cortical actin thickening in non-polarised mitotic mammary epithelial cells acts as a compensatory mechanism that allows cells to overcome loss of tensions and traction forces that polarised cells receive through E-cadherin, from neighbouring cells and the epithelial tissue layer. Consistent with this hypothesis, we show that polarised cells have a thinner F-actin cortex and adopt an elongated shape that is defined by neighbouring cells throughout mitosis, where the mitotic spindle aligns along the longest axis of the cell. E-cadherin interacts with actin to sense external mechanical forces and mediate their transduction into intercellular signalling (Buckley et al., 2014; Iskratsch et al., 2014; Lecuit and Yap, 2015; Yonemura et al., 2010). Loss of E-cadherin impairs F-actin integrity, which contributes to morphological changes that induce epithelial-to-mesenchymal transition (EMT) (Chen et al., 2014), consistent with our observations showing that cells failing to assemble cell-cell adhesions acquire a mesenchymal behaviour. E-cadherin acts through myosin 10 to reduce cortical actomyosin contractility to ensure correct mitotic spindle assembly and centrosome dynamics and maintain epithelial integrity (Hidalgo-Carcedo et al., 2011; Rhys et al., 2018). Vinculin has been shown to connect E-cadherin to F-actin at adherens junctions to coordinate mitotic rounding with epithelial integrity maintenance (Monster et al., 2021). Interestingly, in our study, fast and efficient rounding-up of non-polarised mammary epithelial cells did not prevent defects in mitotic spindle dynamics or mitosis progression and outcome. This is again different from findings in HeLa cells showing that efficient cell rounding ensures correct mitotic spindle assembly and chromosome segregation (Serres et al., 2020). This further points to the crosstalk between mitotic mammary epithelial cells and their neighbouring cells, through E-cadherin, to coordinate cell-cell adhesion with correct cortical actin re-organisation and mitotic mechanics. Consistent with this idea,

rounding mitotic MDCK cells generate pushing forces against tissue confinement to create space necessary for their division and proper mitotic spindle orientation and chromosome segregation (Sorce et al., 2015). Reciprocally, maintenance of cell-cell adhesion integrity allows neighbouring cells to exert tensions and traction forces that fine-tune mitotic cell rounding for correct mitosis mechanics and progression (Chanet et al., 2017; Lancaster et al., 2013; Sorce et al., 2015).

Correct crosstalk between actin and astral microtubules at the cell cortex is crucial for generating balanced cortical forces that ensure proper assembly and alignment of the mitotic spindle, as well as for coordinating of chromosome segregation with cytokinesis to ensure error-free cell divisions (Dogterom and Koenderink, 2019; Lechler and Mapelli, 2021; van Leen et al., 2020). In addition to the effects on cortical F-actin rearrangement in non-polarised cells, our experiments reveal an increase in the length of astral microtubules, indicating their stabilisation. This results in mitotic spindle misorientation and excessive oscillations which persist during anaphase. The increase in mitotic spindle length in non-polarised cells did not rescue spindle and chromatid centring defects, which is again different from findings in HeLa cells where larger mitotic spindles are centrally placed in cells undergoing asymmetric plasma membrane elongation to ensure the separation of equal-sized daughter cells at cytokinesis (Kiyomitsu and Cheeseman, 2013). Our results showing several defects in mitotic spindle assembly upon perturbation of cell-cell adhesion formation, could explain the high incidence of chromosome miss-segregation and delayed mitotic progression. We also propose that our observed defects in mitotic spindle dynamics in non-polarised cells are likely due to the thinning of the subcortical actin cloud, which has been shown to associate with retraction fibres and regulate the growth of astral microtubules and their interaction with cortical actin during mitosis (Inoue et al., 2019; Kwon et al., 2015; Yu et al., 2019). The vesicle-bound NDP52 has been shown to regulate the dynamics of the subcortical actin ring, which in turn acts on the growth of astral microtubules to regulate LGN-mediated mitotic spindle orientation, and precise chromosome segregation (Yu et al., 2019). Similarly, the myosin 10 motor protein associates with astral microtubules and works in parallel with Dynein to regulate microtubule dynamic interaction with the cortex and orient centrosomes towards the subcortical actin cloud during mitosis (Kwon et al., 2015). During planar cell division, astral microtubule plus-ends are coupled to E-cadherin junctions that are associated with the actin cortex (Dogterom and Koenderink, 2019). E-cadherin senses tensile forces from neighbouring cells at adherens junctions to pattern LGN at the cell cortex (Gloerich et al., 2017; Hart et al., 2017), while Afadin concomitantly interacts with F-actin and LGN to regulate cortical F-actin re-organisation (Carminati et al., 2016), thereby promoting polarised cortical recruitment of Dynein and anchoring of astral microtubules. Future studies will be key to characterise actin- and microtubule-associated proteins and crosslinkers that regulate the dynamics of F-actin and astral microtubules and their crosstalk in mitotic mammary epithelial cells and determine how their function is coordinated with cell-cell adhesion.

Here we propose a mechanism whereby the membrane-associated S100A11 protein acts as a molecular sensor of external cues linking plasma membrane remodelling to E-cadherin-dependent cell adhesion to coordinate cortex rearrangement and LGN-mediated mitotic spindle dynamics, for correct progression and outcome of mammary epithelial cell divisions. Importantly, we show that S100A11 knockdown phenocopies the effect of perturbation of cell-cell adhesion formation in low-density cultures on plasma membrane remodelling and mitosis progression and outcome. Our observations showing S100A11 and E-cadherin co-localisation at the cell surface in polarised cells and their co-accumulation in the cytoplasm upon perturbation of cell-cell adhesion formation further points to a key role of S100A11 in coordinating the interplay between plasma membrane remodelling and E-cadherin function. Consistent with this, we reveal that S100A11 knockdown abrogates the polarised clustering of E-cadherin to the lateral cortex and impairs adherens junction formation, affecting cell shape of mitotic and interphase mammary epithelial cells. Our observations that S100A11 depletion impairs cortical actin and astral microtubule organisation – which results in off-centred mitotic spindles in metaphase – also suggest that S100A11 function in the regulation of plasma membrane remodelling and cell-cell adhesion integrity is crucial for the previously described role of E-cadherin in directing localised re-organisation of F-actin and astral microtubules and their crosstalk at the sites of adherens junctions (Dogterom and Koenderink, 2019), to ensure correct assembly and positioning of the mitotic spindle. In the presence of Ca^{2+}, S100A11 binds directly to actin to inhibit actin-activated myosin ATPase activity of smooth muscle cells, indicating a key role of S100A11 in the regulation of actin-myosin-mediated contractility (Zhao et al., 2000). S100A11 also associates to microtubules of keratinocytes, which facilitates its translocation to the plasma membrane in a Ca^{2+}-dependent manner (Eckert et al., 2004). Thus, we cannot rule out a direct effect of S100A11 on cortical actin and astral microtubules. Nonetheless, our immunoprecipitation experiments reveal that S100A11 forms a complex with E-cadherin and LGN in mitotic mammary epithelial cells, which corroborates recent proteomics studies showing that S100A11 co-purifies with LGN and E-cadherin in mammary epithelial and MDCK cells, respectively (Fankhaenel et al., 2023; Guo et al., 2014). These findings along with those showing that F-actin complexes with LGN (Carminati et al., 2016), allow us to speculate that S100A11 may be part of the E-cadherin-F-actin-LGN complex to coordinate the crosstalk between adherens junctions, the cell cortex and mitotic machinery. Interestingly, our observations showing loss of the polarised localisation of LGN to the lateral cortex in S100A11-depleted cells suggest that S100A11 is required for LGN cortical patterning rather than its cytoplasm-to-cortex recruitment, consistent with the function of its partner ANXA1 in the regulation of mitotic spindle planar orientation (Fankhaenel et al., 2023). It will be important to further dissect the mitotic functions of the S100A11-ANXA1 complex and its interaction with E-cadherin-F-actin-LGN. Related to this, we show that E-cadherin knockdown abrogates LGN recruitment to the cell cortex and impairs mitotic spindle orientation as described previously (Gloerich et al., 2017; Wang et al., 2018), but does not affect the localisation of

S100A11 to the plasma membrane, further reinforcing the idea that S100A11 acts upstream of E-cadherin to exert its function in mitosis. This also indicates that cell-cell adhesion defect does not solely affect plasma membrane remodelling. Finally, our experiments do not reveal a localisation of S100A11 on the mitotic spindle or chromosomes, indicating that the effect S100A11 depletion on chromosome segregation fidelity is a result of impaired cortical and plasma membrane remodelling, consistent with recent studies linking cortical organisation and cell geometry to faithful chromosome segregation (di Pietro et al., 2017; Knouse et al., 2018; Yu et al., 2019). Together, our findings identify S100A11 as a membrane-associated molecular landmark bridging plasma membrane remodelling, E-cadherin clustering to adherens junctions, cortical actin-astral microtubule dynamic crosstalk and LGN mitotic spindle machinery, for correct orientation, progression, and outcome of mammary epithelial cell divisions. Further mechanistic studies will be key to understand how S100A11 participates in the transduction of external cues into intracellular signalling and determine how this is spatiotemporally coordinated with plasma membrane remodelling and E-cadherin dynamics during mitosis.

In conclusion, our study in mammary epithelial cells reveals an important S100A11-dependent functional, dynamic interplay between the plasma membrane and E-cadherin-mediated cell adhesion to control cortical cytoskeleton re-organisation and LGN-mediated mitotic machinery, thereby ensuring error-free cell divisions and correct shape and positioning of daughter cells. While the plasma membrane is established as a physical interface linking external cues to intracellular signalling during cell division (Rizzelli et al., 2020), our findings point to a key role of the plasma membrane as a molecular platform including components such as S100A11 that act as mechanical sensors controlling the mechanochemical crosstalk between extracellular and intracellular signalling for correct execution of polarised cell divisions. Future work will be important to characterise the proteome and lipidome of the plasma membrane to identify factors that bridge plasma membrane remodelling and epithelial polarity, and to dissect how they coordinate these with the mitotic machinery. Remarkably, our experiments in non-transformed mammary epithelial cells devoid of oncogenic triggers, demonstrate that perturbation of cell-cell adhesion is sufficient to induce mitotic and cytoarchitectural defects that are known as major contributors to developmental disorders and carcinogenesis (Lechler and Mapelli, 2021; Matthews et al., 2020; Taubenberger et al., 2020). Consistent with this, loss of E-cadherin in the normal prostate epithelium results in mitotic spindle and cell behaviour defects that lead to carcinogenesis (Wang et al., 2018). Chromosome instability and chromosome segregation defects have been linked to EMT (Comaills et al., 2016; Matthews et al., 2020; Roschke et al., 2008). Our findings in non-transformed mammary epithelial cells, suggest that perturbation of cell-cell adhesion resulting in impaired epithelial identity represents a key initiating event leading to mitotic spindle dynamics and chromosome segregation defects that are known to drive epithelial malignant transformation (Ramkumar and Baum, 2016). Further studies using 3D cultures and mouse models will be crucial for elucidating how polarised cell divisions are coordinated with

external cues to drive mammary epithelial morphogenesis and carcinogenesis, and for understanding how this is defined by polarised epithelial cell identity.

MATERIALS AND METHODS

Cell lines

MCF-10A cells are spontaneously immortalised, non-transformed human mammary epithelial cells, obtained from ATCC® (#CRL-10317). Cells were cultured in Dulbecco's Modified Eagle Medium/F12 (DMEM/F12, Invitrogen), supplemented with 5% donor horse serum (Gibco), 20 ng/ml human EGF (Sigma #E9644), 0.5 µg/ml Hydrocortisone (Sigma #H0888), 10 µg/ml insulin (Sigma #I1882), 100 ng/ml cholera toxin (Sigma #C8052), 50 U/ml penicillin and 50 µg/ml streptomycin (Life Technologies) and 500 ng/ml Amphotericin B (Gibco #11510496), at 37 °C in a humidified 5% CO_2 atmosphere.

HEK293 cells (ATCC® #CRL-3216) provided by Melissa Andrews (University of Southampton), were cultured in DMEM with high glucose, sodium pyruvate and L-glutamine (Gibco), supplemented with 10% foetal bovine serum (FBS, Gibco) and 50 U/ml penicillin and 50 µg/ml streptomycin (Life Technologies), at 37 °C in a humidified 5% CO_2 atmosphere.

Cell lines were periodically tested for mycoplasma contamination.

siRNAs and transfections

Transient knockdown of S100A11 and E-cadherin in MCF-10A cells was performed by transfection of MISSION® Predesigned (Sigma) or custom-made siRNAs, respectively. To knockdown S100A11, the following siRNAs were used: SASI_Hs01_00164495 (si-S100A11 #1) and SASI_Hs01_00164498 (si-S100A11 #2). To knockdown E-cadherin, the following siRNAs were used: si-Ecadherin#1 (sense: 5'-CAUCUUGACUAGGUAUUGUCU-3'; antisense: 5'-AGACAAUACCUAGUCAAGAUG-3') and si-Ecadherin#2 (sense: 5'-GAGAGAGUUUCCCUACGUAUA-3'; anti-sense: 5'-UAUACGUAGGGAAACUCUCUC-3'). All experiments using siRNAs were carried in the presence of SiGENOME RISC-Free (Dharmacon), used as a negative control for siRNAs experiments (si-Control). MCF-10A cells were transfected with a final concentration of 50 nm of siRNAs diluted in Opti-MEM® Reduced Serum Medium (Gibco) using Lipofectamine™ RNAiMAX (Invitrogen), following the manufacturer's protocol. Transfected cells were incubated for 48 h or 72h, before they were live-imaged, lysed or fixed and immunoprocessed.

Retroviral constructs and generation of stable cell lines

Retroviral constructs were used to transduce MCF-10A cells. Lifeact-mCherry was obtained from Addgene (pTK93_Lifeact-mCherry, #46357). pTK14-GFP-S100A11 was cloned as follows: First,

the human S100A11 sequence was obtained from the NCBI database (reference sequence: NM-005620.2). Then, the S100A11 cDNA flanked by XhoI and SacII restriction digestion sites sequences were synthesized in a pEX-A128 plasmid (Eurofins Scientific). Second, the synthesized S100A11 was removed from the pEX-A128 plasmid by restriction digestion with XhoI and SacII (New England Biolabs), then cloned into a pTK14-GFP plasmid (Fankhaenel et al., 2023). Correct insertion was verified by Sanger sequencing.

Generation of stable MCF-10A cell lines was performed using retroviral transduction. Retroviruses were prepared in HEK293 cells by calcium phosphate co-transfection of 10 µg retroviral plasmid, 5 µg packaging plasmid pUMVC (Addgene, Plasmid #8449), 6.5 µg envelope plasmid pCMV-VSV-G (Addgene, Plasmid #8454). Virus particles were collected 48 h after transfection then filtered through a 0.45 µm syringe filter and used to infect MCF-10A cells in the presence of 8 µg/ml polybrene (Sigma). Clones of interest were selected using 1 µg/ml puromycin (Sigma).

All plasmids and cell lines are available upon request.

Cell cycle synchronization

MCF-10A cells were treated with 9 µM RO-3306 (Sigma #SML0569), dissolved in DMSO, for 18 h to allow CDK1 inhibition and synchronise cells in G2/M phase. To further arrest cells in metaphase, MCF-10A cells were released from the G2/M block by washing three times in pre-warmed drug-free medium and incubated in fresh medium for 35 min.

Cell extracts and immunoblotting

MCF-10A cells were lysed in NP-40 lysis buffer [50 mM Trizma® hydrochloride (Tris-HCl), pH 7.4; 250 mM Sodium Chloride (NaCl); 5 mM Ethylenediaminetetraacetic acid (EDTA); 50 mM Sodium fluoride (NaF); 1 mM Sodium orthovanadate (Na_3VO_4); 1% Nonidet P40 (NP40)], supplemented with protease inhibitor cocktail (Sigma, #P2714). Protein concentration of lysates was determined using Pierce™ BCA Protein Assay (Thermo Scientific). Proteins were subjected to sodium dodecyl sulphate polyacrylamide gel electrophoresis (SDS-PAGE) and subsequent Western blot analysis. The following primary antibodies were used: anti-α-tubulin DM1A (0.2 µg / ml, Sigma #T6199), anti-E-cadherin (1:500, Abcam #ab76055), anti-S100A11 (1:500, Proteintech #10237-1-AP), anti-LGN (1:500, Sigma #ABT174), anti-phospho-Histone3 (0.2 µg / ml, Sigma #06-570) and anti-GFP (2 µg/ml, Invitrogen #A-11122). Secondary antibodies conjugated to horseradish peroxidase (Invitrogen, #32430, #32460) were used at 1:10,000. Proteins were visualised using SuperSignal™ West Pico PLUS Chemiluminescent Substrate (ECL) (Thermo Scientific), followed by imaging using a Syngene PXi detection system Scanner (Syngene).

Immunoprecipitation

Clonal MCF-10A stably expressing pTK14-GFP-S100A11 or pTK14-GFP were plated in 15 cm dishes and washed twice with ice-cold PBS before protein extraction. About 10×10^7 cells were lysed in a mild lysis buffer [50 mM Tris, pH 7.4, 150 mM NaCl, 0.5 mM EDTA, 10 mM NaF, 1 mM Na3VO4, 0.5% Nonidet P40 (NP40)], containing protease inhibitor cocktail. Cell lysates were cleared by centrifugation at 17,000 x *g* for 30 min at 4°C. Co-immunoprecipitation was performed using a GFP-Trap Kit (Chromotek, #gtma-20) following manufacturer's instructions. For immunoblotting, washed beads were eluted by boiling in Laemmli sample buffer (Bio-Rad) containing 5% 2-mercaptoethanol.

Immunofluorescence

The following primary antibodies were used: anti-E-cadherin (1:200, Fisher, #13-1900), anti-S100A11 (10 μg/ml, Proteintech #10237-1-AP), anti-LGN (1:200, Sigma #ABT174), anti-α-tubulin DM1A (1 μg/ml, Sigma #T6199), anti-γ-tubulin AK-15 (1:300, Sigma #T3320). AlexaFluor555 phalloidin (1:50, Life Technologies #A34055) was used to label F-actin. Secondary antibodies (Life Technologies) used were goat anti-mouse (#A-32723 and #A-21125), anti-rabbit (#A-11037 and #A-11008) and anti-rat (#A-11007) conjugated to AlexaFluor488, AlexaFluor594 or AlexaFluor647, at 5 μg/ml.

To visualise α-tubulin and γ-tubulin, MCF-10A cells were fixed in ice-cold anhydrous methanol (Sigma) for 5 minutes followed by fixation with 4% paraformaldehyde (PFA, Fisher) for 10 min. PFA was prepared in PHEM [60 mM Piperazine-1,4-bis(2-ethanesulfonic acid) (PIPES), 25 mM 4-(2-hydroxyethyl)-1-piperazineethanesulfonic acid (HEPES), 10 mM ethylene glycol-bis(β-aminoethyl ether)-N,N,N′,N′-tetraacetic acid (EGTA), and 4 mM Magnesium Sulphate (MgSO4)], diluted in PBS. Cells were washed with PBS, then permeabilised with 0.1% Triton X-100-PBS (Sigma) for 10 min. Cells were blocked with 10% goat serum (Sigma) and 1% Bovine Serum Albumin (BSA, Sigma) in 0.1% Triton X-100-PBS for 1 h. To visualise E-cadherin, S100A11 and LGN, cells were fixed in ice-cold anhydrous methanol for 10 minutes. Cells were then washed with PBS and incubated in 10% goat serum and 1% BSA in 0.1% Triton X-100-PBS for 1 h. To visualise cortical F-actin and astral microtubules, cells were fixed 10 min in 3% PFA and 0.25% Glutaraldehyde (Sigma) in 0.2% NP-40 (Sigma) diluted in Brinkley Buffer 1980 (BRB80) [80 mM PIPES, 1 mM Magnesium Chloride (MgCl2), hexahydrate and 1 mM EGTA diluted in dH2O]. Cells were blocked in 0.1% ammonium chloride (NH_4Cl) (Sigma) in BRB80 for 10 min, followed by two washes in BRB80 for 5 min each. Cells were then blocked in 3% BSA in 0.2% NP-40-BRB80. For all immunostaining, cells were incubated with primary antibodies at 4°C overnight. Cells were washed and incubated with appropriate secondary antibodies for 1 h at RT. Finally, cells were counterstained with 25 μg/ml Hoechst 33342 (Sigma) and mounted with Vectashield antifade mounting medium (Vector Laboratories).

Quantitative confocal microscopy

Immunofluorescence images were captured with an inverted Leica TCS SP8 inverted laser scanning microscope (Leica Microsystems) using a 63x glycerol immersion (63x HC Plan/Apo CS2 1.30 NA) objective. *Z*-stacks at 16-bit depth and 2048 × 2048 pixels were collected at 0.2 or 0.3 µm intervals. Images were processed with Fiji software (Schindelin et al., 2012). Astral microtubule images were denoised using the MATLAB-based ND-Safir software(Boulanger et al., 2010).

Cortical fluorescence intensity of E-cadherin in metaphase cells was measured in Fiji using a custom macro as described in (di Pietro et al., 2017). The macro measured the pixel value at the cell cortex providing 180 measurements with 2-degree intervals around the defined cell cortex. Fluorescence intensity values were reported along the cortex starting (and finishing) from a point facing the metaphase plate. For measurements along the *xy* axis, position 0 and 180 face the chromosome plate (central cortex) and position 90 and 270 face the spindle poles (lateral cortex): 180 positions were scanned (every 2°) along the cortex. Along the *z* axis, positions 0^o and 360^o indicate the apical cortex, 90^o and 270^o indicate the lateral cortex, and 180^o indicates the basal cortex. To account for more elongated cell shapes, a line was drawn along the cell contour using the Freehand tool and the macro fits an ellipse to this contour. Fluorescence intensities were calculated along a 30 pixel-long radial line overlapping the cortex and the maximum intensity was reported. Fluorescence was measured around a 10-pixel perpendicular line along the cortex. Measurements were taken at 280 positions, starting from the short axis of the ellipse. Background values were subtracted from all measured fluorescence intensities.

To measure relative fluorescence intensities of E-cadherin and S100A11 at the cell cortex and cytoplasm, a 30-pixel line was drawn across the lateral surface and the cytoplasm using Fiji software. The line scan function of Fiji was used to reveal the relative fluorescence intensity across the line.

Measurement of F-actin fluorescence intensities was performed on 8-bit images, generating a selection for measuring total F-actin fluorescence intensity ($I_{\text{total actin}}$). Cortical F-actin ($I_{\text{cortical actin}}$) was measured similarly, with the use of the freehand tool to draw around the cortex of the cell. Subcortical F-actin fluorescence intensity ($I_{\text{subcortical actin}}$) was determined by subtracting cortical F-actin fluorescence from total F-actin fluorescence. Background values were subtracted for correct F-actin fluorescence intensity measurement on maximum projection images. Actin cloud penetration length was measured by drawing a line between the sub-cortical and spindle poles areas at both sides of the cell poles, and then an average value was calculated. Quantification of F-actin organisation at adherens junctions was performed by analysing the clustering of F-actin at sites of cell-cell contacts, which was defined by the formation of F-actin bundles.

Like F-actin, total, plasma membrane and cytoplasmic S100A11 fluorescence intensities were measured. Ratio of plasma membrane-to-cytoplasmic S100A11 fluorescence intensities was

measured using Fiji software. Maximum projections of images were generated and the fluorescence intensity of the whole cell (I_{total}) and the cytoplasm ($I_{cytoplasm}$) were measured. Background signal was subtracted, and the plasma membrane-to-cytoplasm fluorescence intensity ratio of S100A11 ($I_{plasma\ membrane}/I_{cytoplasm}$) was calculated as $I_{plasma\ membrane}/I_{cytoplasm} = (I_{total} - I_{cytoplasm})/ I_{cytoplasm}$.

Astral microtubule intensity (α-tubulin signal) was measured using Fiji software. Maximum projections of images were generated and the fluorescence intensity of the whole cell (I_{total}) and the spindle ($I_{spindle}$) excluding spindle poles with astral microtubules were measured. Background signal was subtracted, and the relative fluorescence intensity of astral microtubules ($I_{astral,\ rel}$) was calculated as $I_{astral,\ rel} = (I_{total} - I_{spindle})/I_{spindle}$. Length of astral microtubules was measured by drawing a line along the astral microtubule extending towards the cell cortex on both sides of the poles. Similarly, the pole-to-cortex distance was measured by drawing a line towards the closest cell cortex in line with the spindle axis.

Cell segmentation and quantification of cell morphology were performed in cells stained for E-cadherin using the Fiji MorphoLibJ plugin as described in (Legland et al., 2016). Cell height was quantified in Fiji by drawing a straight line between the apical and basal membranes of cells viewed along the *z* axis.

Mitotic spindle orientation was measured using Fiji in metaphase cells stained for γ-tubulin. The spindle axis was defined by drawing a 30-pixel wide line across both spindle poles and repositioned along the *z* axis. The spindle axis angle α*z* was measured in respect to the substratum using the angle tool.

Quantitative live cell imaging

MCF-10A, GFP-S100A11- or Lifeact-mCherry-expressing cells lines were plated in 27 mm Glass Bottom Dishes (Nunc). Prior to imaging, cells were incubated in cell culture medium supplemented with 100 ng/ml Hoechst 33342 (Sigma) for 30 minutes to visualise DNA. When the plasma membrane or mitotic spindles were observed, cells were further incubated in cell culture medium supplemented with CellMask™ Deep Red Plasma Membrane Stain (Thermo Scientific # C10046) at 1:1000 dilution for 10 minutes or with 100 nM SiR-tubulin (Spirochrome #251SC002) for 3 h. Cells were imaged at 37 °C in CO_2 independent medium (Gibco) using a DeltaVision Elite microscope (GE Healthcare) coupled to a sCMOS max chip area 2048 × 2048 camera (G.E. Healthcare). For each recording, image stacks at 0.6 µm increments in 1,024 x 1,024 format were acquired using a PlanApo 60x/1.42 Oil immersion objective (Olympus) with 2 × 2 binning. Images were taken at 3 stage positions every 3 min for 3 or 5 h. Exposure times were 200 msec and 5% laser power for GFP, 50 msec and 2% laser power for mCherry, 80 msec and 2% laser power for labelled DNA and microtubules, and 50 msec and 2% laser power for labelled plasma membrane

using the DAPI-FITC-mCh-Cy5 filter set. Images were deconvolved using the DeltaVision software SoftWoRx and further processed using Fiji.

Plasma membrane dynamic remodelling was visualised by following the distribution CellMask^{TM} labelling at the cell surface in successive timeframes, where it displayed circumferential, unilateral, or bilateral accumulation in mitotic cells. Plasma membrane elongation was quantified by merging images of anaphase and telophase using Fiji software. Then, elongation of the plasma membrane at the cell cortex of the newly formed daughter cells was assessed. Equal membrane elongation of the newly generated cells is considered symmetric elongation, whereas unequal elongation is considered asymmetric elongation. Measurement of daughter cells' area expressed in μm^2 was performed using the freehand tool in Fiji to highlight the cortex of daughter cells at cytokinesis. Ratio of daughter cell area was calculated by dividing the largest cell area by the smallest cell area. Chromosome-to-cell cortex distance was measured by drawing a line from the middle of the sister chromatid cluster to the polar cell cortex during telophase using the line tool in Fiji. Ratio of chromosome-to-cell cortex distance was calculated by dividing the longest distance by the shortest distance for each cell at telophase. The number of blebs during anaphase-to-telophase transition was determined using the 3D objects counter tool in Fiji.

Oscillations of the mitotic spindle were calculated from time-lapse videos of cells labelled with SiR-tubulin and Hoechst 33342. Metaphase spindle angles in the *z* (α*z*) and *xy* (α*xy*) planes were manually determined for every frame using Fiji software. Measurements of the spindle angle axis in the *z* plane were performed as described above in fixed cells. Spindle angles were reported as positive values unless spindle poles changed direction. In this case, angles were displayed as negative values. Mitotic spindle orientation in the *xy* plane was measured by drawing a line crossing both spindle poles of the first frame of metaphase. This line was embedded to all the following frames to mark the initial position of the mitotic spindle. In the next frame, another line was overlaid across the poles to define the new spindle axis. The angle between the initial spindle position and the current spindle axis was measured using the angle tool. Spindle movement directions were considered by reporting spindle rotations clockwise as positive angles and reverse movements as negative angles. Spindle angle deviations greater than 10° between two frames were counted as oscillations. The oscillation index was determined as the percentage of oscillations in respect to the total number of frames.

Quantification of actin fluorescence from time-lapse videos of Lifeact-mCherry-expressing cells in prometaphase and metaphase was performed as described in (Mahlandt and Goedhart, 2022). Ratios of prometaphase-to-metaphase total, cortical and subcortical actin were calculated. Cell morphology and roundness (4*area/pi*sqr(major axis)) quantification was performed using the shape descriptors plugin in Fiji. Rounding timing was determined by analysing successive frames of the time-lapse videos. The full width at half maximum (FWHM) of cortex intensity profiles to assess the thickness of cortical actin. A straight line with the same length was drawn across the

cortical actin in all data analysed (cortical actin was centred at the middle of the line). Then, a plot profile was generated using Fiji, and the FWHM calculated using Origin(Pro) Version 2021b (https://www.originlab.com/2021).

Statistical analysis

All statistical analysis were performed with GraphPad Prism 9.1.2 software. Graphs were created using GraphPad Prism 9.1.2 software and RStudio (1.2.5033 version). Multiple groups were tested using analysis of variance (ANOVA) with post hoc Tukey or Dunnett tests, and comparisons between two groups were performed using *t*-tests. Data are shown as mean ± standard error of the mean (s.e.m.) from three or four independent experiments. $P \leq 0.05$ was considered statistically significant. Asterisks indicate levels of significance (*$P \leq 0.05$; **$P \leq 0.01$; ***$P \leq 0.001$; ****$P \leq 0.0001$). More specific details about the number of experiments and objects counted, and statistical tests performed are indicated in the figure legends.

Acknowledgments

We would like to thank Dr. Mark Willett at the Imaging and Microscopy Centre for valuable assistance with fluorescence microscopy and Dr. Melissa Andrews for providing the HEK293 cell line. Cartoons in the main and supplementary figures were created using BioRender.com.

Competing interests

The authors declare no competing or financial interests.

Author Contributions

MMH designed and performed experiments, analysed, and interpreted the data. JC performed experiments and analysed the data. MF performed experiments. MRP designed experiments and supervised MMH. SE conceived and designed the project, performed experiments, analysed, and interpreted the data, supervised MMH and wrote the manuscript with the help of MMH. All the authors provided intellectual input, edited, and approved the final manuscript.

Funding

This work was supported by a Wellcome Trust Seed Award in Science (210077/Z/17/Z) and MRC New Investigator Research Grant (MR/R026610/1) awarded to SE. MMH was supported by a Kingdom of Saudi Arabia Ministry of Education PhD studentship.

Data availability

All relevant data can be found within the article and its supplementary information.

References

Baker, J. and Garrod, D. (1993). Epithelial cells retain junctions during mitosis. *J Cell Sci* **104 (Pt 2)**, 415-25.

Bosveld, F., Markova, O., Guirao, B., Martin, C., Wang, Z., Pierre, A., Balakireva, M., Gaugue, I., Ainslie, A., Christophorou, N. et al. (2016). Epithelial tricellular junctions act as interphase cell shape sensors to orient mitosis. *Nature* **530**, 495-8.

Boulanger, J., Kervrann, C., Bouthemy, P., Elbau, P., Sibarita, J. B. and Salamero, J. (2010). Patch-based nonlocal functional for denoising fluorescence microscopy image sequences. *IEEE Trans Med Imaging* **29**, 442-54.

Box, K., Joyce, B. W. and Devenport, D. (2019). Epithelial geometry regulates spindle orientation and progenitor fate during formation of the mammalian epidermis. *Elife* **8**.

Buckley, C. D., Tan, J., Anderson, K. L., Hanein, D., Volkmann, N., Weis, W. I., Nelson, W. J. and Dunn, A. R. (2014). Cell adhesion. The minimal cadherin-catenin complex binds to actin filaments under force. *Science* **346**, 1254211.

Carlton, J. G., Jones, H. and Eggert, U. S. (2020). Membrane and organelle dynamics during cell division. *Nat Rev Mol Cell Biol* **21**, 151-166.

Carminati, M., Gallini, S., Pirovano, L., Alfieri, A., Bisi, S. and Mapelli, M. (2016). Concomitant binding of Afadin to LGN and F-actin directs planar spindle orientation. *Nat Struct Mol Biol* **23**, 155-63.

Chaigne, A., Smith, M. B., Lopez Cavestany, R., Hannezo, E., Chalut, K. J. and Paluch, E. K. (2021). Three-dimensional geometry controls division symmetry in stem cell colonies. *J Cell Sci* **134**.

Chanet, S., Sharan, R., Khan, Z. and Martin, A. C. (2017). Myosin 2-Induced Mitotic Rounding Enables Columnar Epithelial Cells to Interpret Cortical Spindle Positioning Cues. *Curr Biol* **27**, 3350-3358 e3.

Chen, A., Beetham, H., Black, M. A., Priya, R., Telford, B. J., Guest, J., Wiggins, G. A., Godwin, T. D., Yap, A. S. and Guilford, P. J. (2014). E-cadherin loss alters cytoskeletal organization and adhesion in non-malignant breast cells but is insufficient to induce an epithelial-mesenchymal transition. *BMC Cancer* **14**, 552.

Chiu, C. W. N., Monat, C., Robitaille, M., Lacomme, M., Daulat, A. M., Macleod, G., McNeill, H., Cayouette, M. and Angers, S. (2016). SAPCD2 Controls Spindle Orientation and Asymmetric Divisions by Negatively Regulating the Galphai-LGN-NuMA Ternary Complex. *Dev Cell* **36**, 50-62.

Comaills, V., Kabeche, L., Morris, R., Buisson, R., Yu, M., Madden, M. W., LiCausi, J. A., Boukhali, M., Tajima, K., Pan, S. et al. (2016). Genomic Instability Is Induced by Persistent Proliferation of Cells Undergoing Epithelial-to-Mesenchymal Transition. *Cell Rep* **17**, 2632-2647.

di Pietro, F., Echard, A. and Morin, X. (2016). Regulation of mitotic spindle orientation: an integrated view. *EMBO Rep* **17**, 1106-30.

di Pietro, F., Valon, L., Li, Y., Goiame, R., Genovesio, A. and Morin, X. (2017). An RNAi Screen in a Novel Model of Oriented Divisions Identifies the Actin-Capping Protein Z beta as an Essential Regulator of Spindle Orientation. *Curr Biol* **27**, 2452-2464 e8.

Dix, C. L., Matthews, H. K., Uroz, M., McLaren, S., Wolf, L., Heatley, N., Win, Z., Almada, P., Henriques, R., Boutros, M. et al. (2018). The Role of Mitotic Cell-Substrate Adhesion Re-modeling in Animal Cell Division. *Dev Cell* **45**, 132-145 e3.

Dogterom, M. and Koenderink, G. H. (2019). Actin-microtubule crosstalk in cell biology. *Nat Rev Mol Cell Biol* **20**, 38-54.

Donker, L., Houtekamer, R., Vliem, M., Sipieter, F., Canever, H., Gomez-Gonzalez, M., Bosch-Padros, M., Pannekoek, W. J., Trepat, X., Borghi, N. et al. (2022). A mechanical G2 checkpoint controls epithelial cell division through E-cadherin-mediated regulation of Wee1-Cdk1. *Cell Rep* **41**, 111475.

Eckert, R. L., Broome, A. M., Ruse, M., Robinson, N., Ryan, D. and Lee, K. (2004). S100 proteins in the epidermis. *J Invest Dermatol* **123**, 23-33.

Fankhaenel, M., Hashemi, F. S. G., Mourao, L., Lucas, E., Hosawi, M. M., Skipp, P., Morin, X., Scheele, C. and Elias, S. (2023). Annexin A1 is a polarity cue that directs mitotic spindle orientation during mammalian epithelial morphogenesis. *Nat Commun* **14**, 151.

Gloerich, M., Bianchini, J. M., Siemers, K. A., Cohen, D. J. and Nelson, W. J. (2017). Cell division orientation is coupled to cell-cell adhesion by the E-cadherin/LGN complex. *Nat Commun* **8**, 13996.

Guo, Z., Neilson, L. J., Zhong, H., Murray, P. S., Zanivan, S. and Zaidel-Bar, R. (2014). E-cadherin interactome complexity and robustness resolved by quantitative proteomics. *Sci Signal* **7**, rs7.

Hart, K. C., Tan, J., Siemers, K. A., Sim, J. Y., Pruitt, B. L., Nelson, W. J. and Gloerich, M. (2017). E-cadherin and LGN align epithelial cell divisions with tissue tension independently of cell shape. *Proc Natl Acad Sci U S A* **114**, E5845-E5853.

Hertwig, O. (1884). Untersuchungen zur morphologie und physiologie der zelle: Fischer.

Hidalgo-Carcedo, C., Hooper, S., Chaudhry, S. I., Williamson, P., Harrington, K., Leitinger, B. and Sahai, E. (2011). Collective cell migration requires suppression of actomyosin at cell-cell contacts mediated by DDR1 and the cell polarity regulators Par3 and Par6. *Nat Cell Biol* **13**, 49-58.

Inoue, D., Obino, D., Pineau, J., Farina, F., Gaillard, J., Guerin, C., Blanchoin, L., Lennon-Dumenil, A. M. and Thery, M. (2019). Actin filaments regulate microtubule growth at the centrosome. *EMBO J* **38**.

Iskratsch, T., Wolfenson, H. and Sheetz, M. P. (2014). Appreciating force and shape-the rise of mechanotransduction in cell biology. *Nat Rev Mol Cell Biol* **15**, 825-33.

Jaiswal, J. K., Lauritzen, S. P., Scheffer, L., Sakaguchi, M., Bunkenborg, J., Simon, S. M., Kallunki, T., Jaattela, M. and Nylandsted, J. (2014). S100A11 is required for efficient plasma membrane repair and survival of invasive cancer cells. *Nat Commun* **5**, 3795.

Kiyomitsu, T. and Cheeseman, I. M. (2013). Cortical dynein and asymmetric membrane elongation coordinately position the spindle in anaphase. *Cell* **154**, 391-402.

Knouse, K. A., Lopez, K. E., Bachofner, M. and Amon, A. (2018). Chromosome Segregation Fidelity in Epithelia Requires Tissue Architecture. *Cell* **175**, 200-211 e13.

Kwon, M., Bagonis, M., Danuser, G. and Pellman, D. (2015). Direct Microtubule-Binding by Myosin-10 Orients Centrosomes toward Retraction Fibers and Subcortical Actin Clouds. *Dev Cell* **34**, 323-37.

Lancaster, O. M., Le Berre, M., Dimitracopoulos, A., Bonazzi, D., Zlotek-Zlotkiewicz, E., Picone, R., Duke, T., Piel, M. and Baum, B. (2013). Mitotic rounding alters cell geometry to ensure efficient bipolar spindle formation. *Dev Cell* **25**, 270-83.

Lechler, T. and Fuchs, E. (2005). Asymmetric cell divisions promote stratification and differentiation of mammalian skin. *Nature* **437**, 275-80.

Lechler, T. and Mapelli, M. (2021). Spindle positioning and its impact on vertebrate tissue architecture and cell fate. *Nat Rev Mol Cell Biol* **22**, 691-708.

Lecuit, T. and Yap, A. S. (2015). E-cadherin junctions as active mechanical integrators in tissue dynamics. *Nat Cell Biol* **17**, 533-9.

Legland, D., Arganda-Carreras, I. and Andrey, P. (2016). MorphoLibJ: integrated library and plugins for mathematical morphology with ImageJ. *Bioinformatics* **32**, 3532-3534.

Leguay, K., Decelle, B., Elkholi, I. E., Bouvier, M., Cote, J. F. and Carreno, S. (2022). Interphase microtubule disassembly is a signaling cue that drives cell rounding at mitotic entry. *J Cell Biol* **221**.

Lukinavicius, G., Reymond, L., D'Este, E., Masharina, A., Gottfert, F., Ta, H., Guther, A., Fournier, M., Rizzo, S., Waldmann, H. et al. (2014). Fluorogenic probes for live-cell imaging of the cytoskeleton. *Nat Methods* **11**, 731-3.

Mahlandt, E. K. and Goedhart, J. (2022). Visualizing and Quantifying Data from Time-Lapse Imaging Experiments. In *Fluorescent Microscopy*, pp. 329-348: Springer.

Matsumura, S., Hamasaki, M., Yamamoto, T., Ebisuya, M., Sato, M., Nishida, E. and Toyoshima, F. (2012). ABL1 regulates spindle orientation in adherent cells and mammalian skin. *Nat Commun* **3**, 626.

Matthews, H. K., Delabre, U., Rohn, J. L., Guck, J., Kunda, P. and Baum, B. (2012). Changes in Ect2 localization couple actomyosin-dependent cell shape changes to mitotic progression. *Dev Cell* **23**, 371-83.

Matthews, H. K., Ganguli, S., Plak, K., Taubenberger, A. V., Win, Z., Williamson, M., Piel, M., Guck, J. and Baum, B. (2020). Oncogenic Signaling Alters Cell Shape and Mechanics to Facilitate Cell Division under Confinement. *Dev Cell* **52**, 563-573 e3.

Mohammed, T. O., Lin, Y.-R., Weissenbruch, K., Ngo, K. X., Zhang, Y., Kodera, N., Bastmeyer, M., Miyanari, Y., Taoka, A. and Franz, C. M. (2023). S100A11 promotes focal adhesion disassembly via myosin II-driven contractility and Piezo1-mediated Ca2+ entry. *bioRxiv*, 2023.07.17.549432.

Monster, J. L., Donker, L., Vliem, M. J., Win, Z., Matthews, H. K., Cheah, J. S., Yamada, S., de Rooij, J., Baum, B. and Gloerich, M. (2021). An asymmetric junctional mechanoresponse coordinates mitotic rounding with epithelial integrity. *J Cell Biol* **220**.

Narayanan, P., Chatterton, P., Ikeda, A., Ikeda, S., Corey, D. P., Ervasti, J. M. and Perrin, B. J. (2015). Length regulation of mechanosensitive stereocilia depends on very slow actin dynamics and filament-severing proteins. *Nat Commun* **6**, 6855.

Nestor-Bergmann, A., Stooke-Vaughan, G. A., Goddard, G. K., Starborg, T., Jensen, O. E. and Woolner, S. (2019). Decoupling the Roles of Cell Shape and Mechanical Stress in Orienting and Cueing Epithelial Mitosis. *Cell Rep* **26**, 2088-2100 e4.

Okumura, M., Natsume, T., Kanemaki, M. T. and Kiyomitsu, T. (2018). Dynein-Dynactin-NuMA clusters generate cortical spindle-pulling forces as a multi-arm ensemble. *Elife* **7**.

Ozlu, N., Qureshi, M. H., Toyoda, Y., Renard, B. Y., Mollaoglu, G., Ozkan, N. E., Bulbul, S., Poser, I., Timm, W., Hyman, A. A. et al. (2015). Quantitative comparison of a human cancer cell surface proteome between interphase and mitosis. *EMBO J* **34**, 251-65.

Pirovano, L., Culurgioni, S., Carminati, M., Alfieri, A., Monzani, S., Cecatiello, V., Gaddoni, C., Rizzelli, F., Foadi, J., Pasqualato, S. et al. (2019). Hexameric NuMA:LGN structures promote multivalent interactions required for planar epithelial divisions. *Nat Commun* **10**, 2208.

Prosser, S. L. and Pelletier, L. (2017). Mitotic spindle assembly in animal cells: a fine balancing act. *Nat Rev Mol Cell Biol* **18**, 187-201.

Ragkousi, K. and Gibson, M. C. (2014). Cell division and the maintenance of epithelial order. *J Cell Biol* **207**, 181-8.

Ramkumar, N. and Baum, B. (2016). Coupling changes in cell shape to chromosome segregation. *Nat Rev Mol Cell Biol* **17**, 511-21.

Reinsch, S. and Karsenti, E. (1994). Orientation of spindle axis and distribution of plasma membrane proteins during cell division in polarized MDCKII cells. *J Cell Biol* **126**, 1509-26.

Rhys, A. D., Monteiro, P., Smith, C., Vaghela, M., Arnandis, T., Kato, T., Leitinger, B., Sahai, E., McAinsh, A., Charras, G. et al. (2018). Loss of E-cadherin provides tolerance to centrosome amplification in epithelial cancer cells. *J Cell Biol* **217**, 195-209.

Rintala-Dempsey, A. C., Rezvanpour, A. and Shaw, G. S. (2008). S100-annexin complexes--structural insights. *FEBS J* **275**, 4956-66.

Rizzelli, F., Malabarba, M. G., Sigismund, S. and Mapelli, M. (2020). The crosstalk between microtubules, actin and membranes shapes cell division. *Open Biol* **10**, 190314.

Roschke, A. V., Glebov, O. K., Lababidi, S., Gehlhaus, K. S., Weinstein, J. N. and Kirsch, I. R. (2008). Chromosomal instability is associated with higher expression of genes implicated in epithelial-mesenchymal transition, cancer invasiveness, and metastasis and with lower expression of genes involved in cell cycle checkpoints, DNA repair, and chromatin maintenance. *Neoplasia* **10**, 1222-30.

Ruckerl, F., Lenz, M., Betz, T., Manzi, J., Martiel, J. L., Safouane, M., Paterski-Boujemaa, R., Blanchoin, L. and Sykes, C. (2017). Adaptive Response of Actin Bundles under Mechanical Stress. *Biophys J* **113**, 1072-1079.

Schindelin, J., Arganda-Carreras, I., Frise, E., Kaynig, V., Longair, M., Pietzsch, T., Preibisch, S., Rueden, C., Saalfeld, S., Schmid, B. et al. (2012). Fiji: an open-source platform for biological-image analysis. *Nat Methods* **9**, 676-82.

Sedzinski, J., Biro, M., Oswald, A., Tinevez, J. Y., Salbreux, G. and Paluch, E. (2011). Polar actomyosin contractility destabilizes the position of the cytokinetic furrow. *Nature* **476**, 462-6.

Segalen, M., Johnston, C. A., Martin, C. A., Dumortier, J. G., Prehoda, K. E., David, N. B., Doe, C. Q. and Bellaiche, Y. (2010). The Fz-Dsh planar cell polarity pathway induces oriented cell division via Mud/NuMA in Drosophila and zebrafish. *Dev Cell* **19**, 740-52.

Serres, M. P., Samwer, M., Truong Quang, B. A., Lavoie, G., Perera, U., Gorlich, D., Charras, G., Petronczki, M., Roux, P. P. and Paluch, E. K. (2020). F-Actin Interactome Reveals Vimentin as a Key Regulator of Actin Organization and Cell Mechanics in Mitosis. *Dev Cell* **52**, 210-222 e7.

Shankar, J., Messenberg, A., Chan, J., Underhill, T. M., Foster, L. J. and Nabi, I. R. (2010). Pseudopodial actin dynamics control epithelial-mesenchymal transition in metastatic cancer cells. *Cancer Res* **70**, 3780-90.

Sorce, B., Escobedo, C., Toyoda, Y., Stewart, M. P., Cattin, C. J., Newton, R., Banerjee, I., Stettler, A., Roska, B., Eaton, S. et al. (2015). Mitotic cells contract actomyosin cortex and generate pressure to round against or escape epithelial confinement. *Nat Commun* **6**, 8872.

Taneja, N., Fenix, A. M., Rathbun, L., Millis, B. A., Tyska, M. J., Hehnly, H. and Burnette, D. T. (2016). Focal adhesions control cleavage furrow shape and spindle tilt during mitosis. *Sci Rep* **6**, 29846.

Taubenberger, A. V., Baum, B. and Matthews, H. K. (2020). The Mechanics of Mitotic Cell Rounding. *Front Cell Dev Biol* **8**, 687.

Thery, M., Jimenez-Dalmaroni, A., Racine, V., Bornens, M. and Julicher, F. (2007). Experimental and theoretical study of mitotic spindle orientation. *Nature* **447**, 493-6.

Uroz, M., Garcia-Puig, A., Tekeli, I., Elosegui-Artola, A., Abenza, J. F., Marin-Llaurado, A., Pujals, S., Conte, V., Albertazzi, L., Roca-Cusachs, P. et al. (2019). Traction forces at the cytokinetic ring regulate cell division and polyploidy in the migrating zebrafish epicardium. *Nat Mater* **18**, 1015-1023.

Uroz, M., Wistorf, S., Serra-Picamal, X., Conte, V., Sales-Pardo, M., Roca-Cusachs, P., Guimera, R. and Trepat, X. (2018). Regulation of cell cycle progression by cell-cell and cell-matrix forces. *Nat Cell Biol* **20**, 646-654.

van Leen, E. V., di Pietro, F. and Bellaiche, Y. (2020). Oriented cell divisions in epithelia: from force generation to force anisotropy by tension, shape and vertices. *Curr Opin Cell Biol* **62**, 9-16.

Wang, X., Dong, B., Zhang, K., Ji, Z., Cheng, C., Zhao, H., Sheng, Y., Li, X., Fan, L., Xue, W. et al. (2018). E-cadherin bridges cell polarity and spindle orientation to ensure prostate epithelial integrity and prevent carcinogenesis in vivo. *PLoS Genet* **14**, e1007609.

Yonemura, S., Wada, Y., Watanabe, T., Nagafuchi, A. and Shibata, M. (2010). alpha-Catenin as a tension transducer that induces adherens junction development. *Nat Cell Biol* **12**, 533-42.

Yu, H., Yang, F., Dong, P., Liao, S., Liu, W. R., Zhao, G., Qin, B., Dou, Z., Liu, Z., Liu, W. et al. (2019). NDP52 tunes cortical actin interaction with astral microtubules for accurate spindle orientation. *Cell Res* **29**, 666-679.

Zhang, X., Bedigian, A. V., Wang, W. and Eggert, U. S. (2012). G protein-coupled receptors participate in cytokinesis. *Cytoskeleton (Hoboken)* **69**, 810-8.

Zhang, X. and Eggert, U. S. (2013). Non-traditional roles of G protein-coupled receptors in basic cell biology. *Mol Biosyst* **9**, 586-95.

Zhao, X. Q., Naka, M., Muneyuki, M. and Tanaka, T. (2000). Ca(2+)-dependent inhibition of actin-activated myosin ATPase activity by S100C (S100A11), a novel member of the S100 protein family. *Biochem Biophys Res Commun* **267**, 77-9.

Zsolnay, V., Katkar, H. H., Chou, S. Z., Pollard, T. D. and Voth, G. A. (2020). Structural basis for polarized elongation of actin filaments. *Proc Natl Acad Sci U S A* **117**, 30458-30464.

Figures

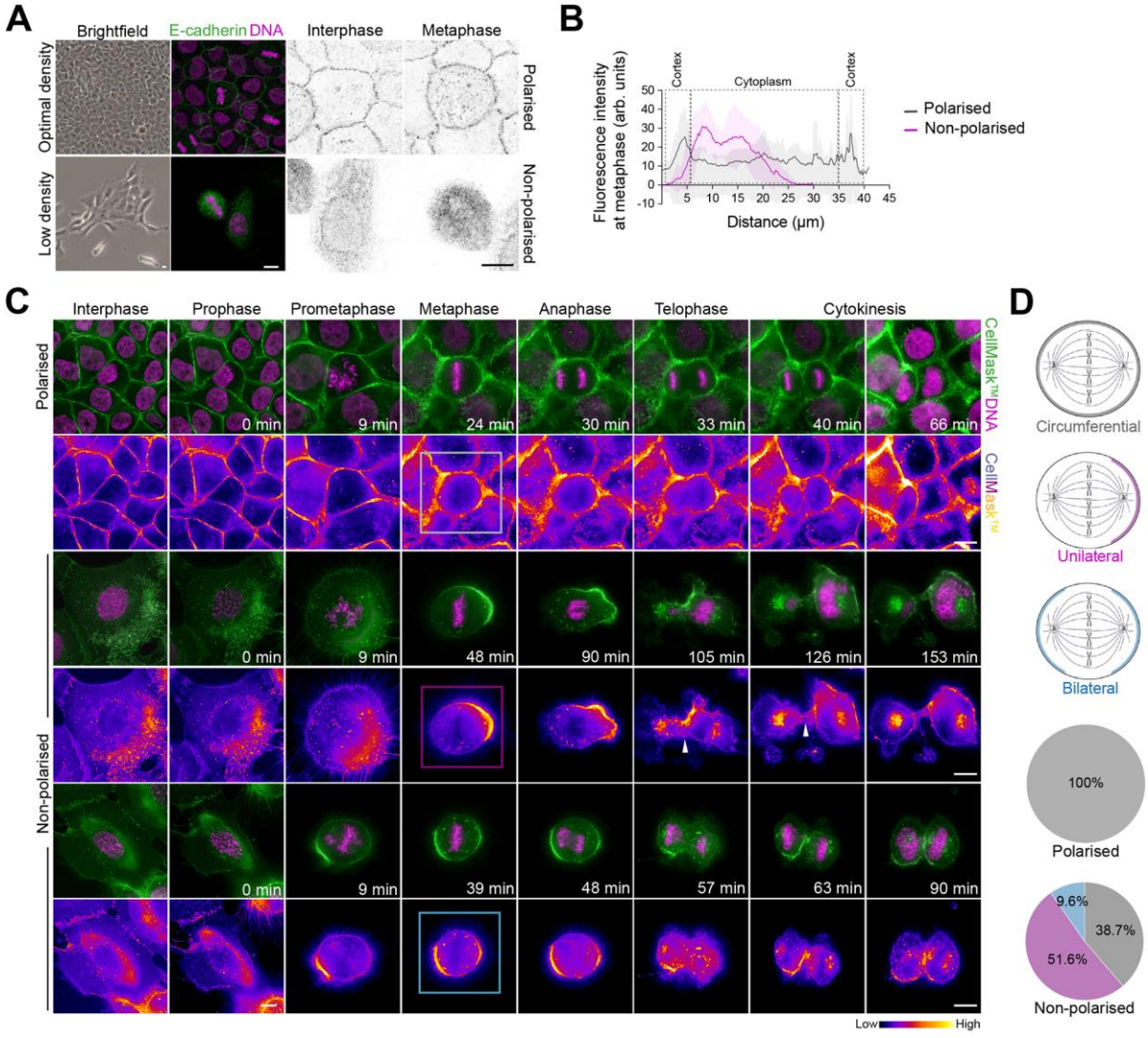

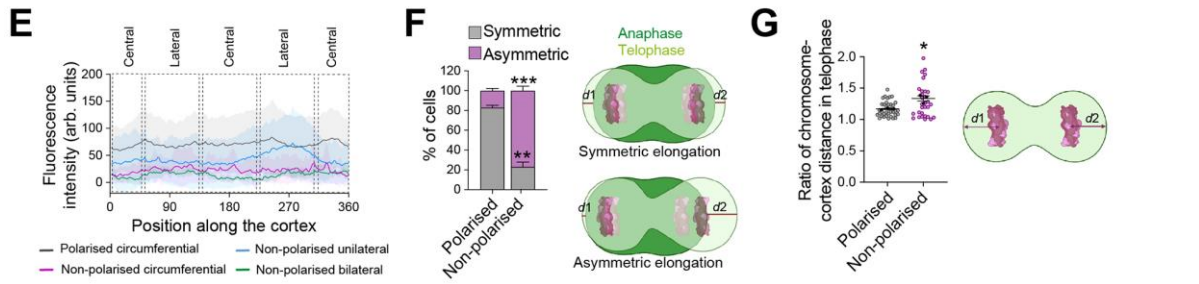

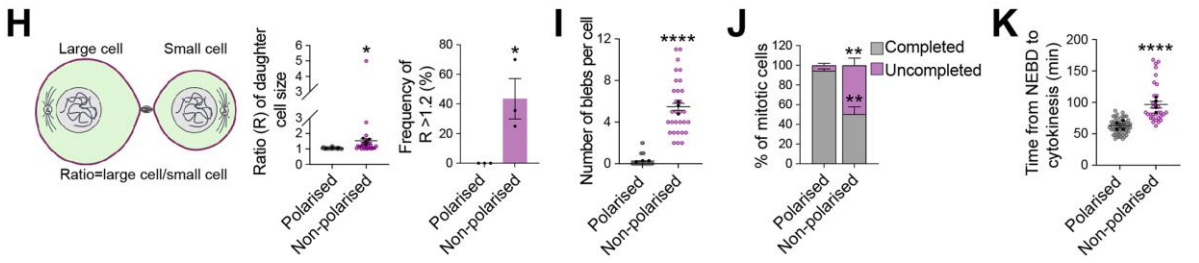

Fig. 1. Perturbation of cell-cell adhesion formation results in asymmetric plasma membrane elongation and defects in mitosis progression and outcome. (A) Confocal images of representative polarised and non-polarised MCF-10A cells stained for E-cadherin (green) and counterstained with Hoechst 33342 (DNA, magenta). **(B)** Average cortical and cytoplasmic fluorescence intensity profiles of E-cadherin in polarised and non-polarised metaphase cells (polarised: *n* = 26 cells; non-polarised: *n* = 24 cells). **(C)** Time-lapse images of representative polarised and non-polarised cells. The plasma membrane is labelled with CellMask™ (green), and DNA with Hoechst 33342 (magenta), 10 min and 30 min before acquisition, respectively. Arrowheads indicate accumulation of vesicles at the cleavage furrow in non-polarised cells. Insets indicate metaphase cells showing the localisation phenotypes of CellMask™ quantified in D: Circumferential (grey); Unilateral (pink); Bilateral (blue). **(D)** Percentage of CellMask™ labelling distribution at the cell surface during metaphase in polarised and non-polarised cells (polarised: *n* = 30 cells; non-polarised: *n* = 30 cells). **(E)** Average cortical fluorescence intensity profiles of CellMask™ from polarised and non-polarised cells (polarised: *n* = 30 cells; non-polarised: *n* = 30 cells). **(F)** Percentage of cells with symmetric and asymmetric plasma membrane elongation, (polarised: *n* = 34 cells; non-polarised: *n* = 32 cells). Distance (*d*) was measured as described on the illustration. Two-sided *t*-test, symmetric: ***P = 0.0003; asymmetric: **P = 0.0012. **(G)** Ratio of chromosome to cortex distance (*d*) in telophase cells (polarised: *n* = 37 cells; non-polarised: *n* = 30 cells). Two-sided t-test, *P = 0.014. *d* was measured as described on the illustration. **(H)** Left: ratio (R) of daughter cell size. *t*-test, *P = 0.018. Right: frequency of R < 1.2. Two-sided *t*-test, *P = 0.0193. (polarised: *n* = 35 cells; non-polarised: *n* = 30 cells). Ratio was measured as described on the illustration. **(I)** Number of polar blebs per cell at anaphase-to-telophase transition (polarised: *n* = 30 cells; non-polarised: *n* = 30 cells). Two-sided *t*-test, ****P < 0.0001. **(J)** Percentage of cells with completed and uncompleted mitosis (polarised: *n* = 63 cells; non-polarised: *n* = 67 cells). Two-sided *t*-test, **P = 0.0013. **(K)** Time from nuclear envelope breakdown (NEBD) to cytokinesis (polarised: *n* = 58 cells; non-polarised: *n* = 34 cells). Two-sided *t*-test, ****P < 0.0001. All data are presented as mean ± s.e.m. from 3 or 4 independent experiments. arb. units (arbitrary units). All scale bars, 10 µm. Source data are provided as a Source Data file.

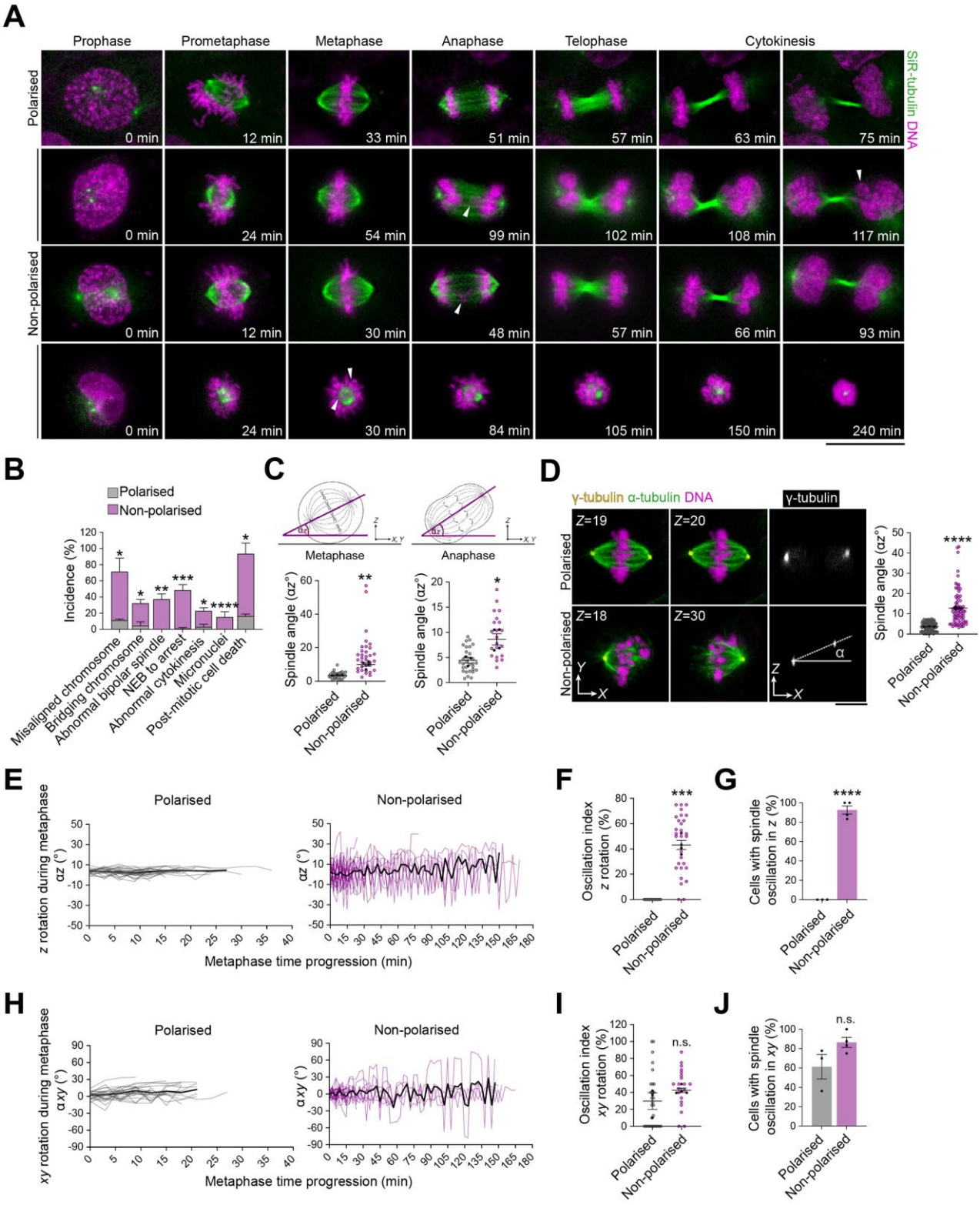

Fig. 2. Perturbation of cell-cell adhesion formation impairs mitotic spindle dynamics and chromosome segregation. (A) Time-lapse images of representative polarised and non-polarised MCF-10A cells. Microtubules are labelled with SiR-tubulin (green) and DNA Hoechst 33342 (magenta), 3 h and 30 min before acquisition, respectively. Arrowheads indicate the phenotypes listed in B. Scale bar, 10 µm. **(B)** Percentage of cells with defects in mitotic spindle assembly, chromosome alignment and segregation, and mitosis progression and outcome (polarised: *n* = 61

cells; non-polarised: *n* = 73 cells). Two-sided *t*-test, misaligned chromosome: **P* = 0.043; bridging chromosome: **P* = 0.029; abnormal bipolar spindle: ***P* = 0.0087; NEB-to-arrest: ****P* = 0.0006; abnormal cytokinesis: **P* = 0.0298; micronuclei: *****P* <0.0001; and post-mitotic cell death: **P* = 0.0462. **(C)** Mitotic spindle angles α*z* from time-lapse images in polarised and non-polarised cells at metaphase (left) (polarised: *n* = 30 cells; non-polarised: *n* = 30 cells); and anaphase (right) (polarised: *n* = 30 cells; non-polarised: *n* = 21 cells). Two-sided *t*-test, metaphase: ***P* = 0.0034; anaphase **P* = 0.0316. **(D)** Left: confocal images of representative polarised and non-polarised cells stained for α-tubulin (green) and anti-γ-tubulin (yellow), and counterstained with Hoechst 33342 (DNA, magenta). Scale bar, 10 µm. Right: mitotic spindle angle α*z* in fixed polarised and non-polarised cells during metaphase (polarised: *n* = 103 cells; non-polarised: *n* = 74 cells). Two-sided *t*-test, *****P* < 0.0001. **(E)** Dynamics of z orientation (α*z*) in polarised cells (left) and non-polarised cells (right), (polarised: *n* = 30 cells; non-polarised: *n* = 30 cells). Black lines represent the average spindle angles. **(F)** Oscillation index in polarised and non-polarised cells, in the *z* axis (polarised: *n* = 30 cells; non-polarised: *n* = 30 cells). Two-sided *t*-test, ****P* = 0.0002. **(G)** Percentage of cells with spindle oscillation in the z axis (polarised: *n* = 30 cells; non-polarised: *n* = 30 cells). Two-sided *t*-test, *****P* < 0.0001. **(H)** Dynamics of *xy* orientation (α*xy*) in polarised cells (left) and non-polarised cells (right), (polarised: *n* = 30 cells; non-polarised: *n* = 28 cells). Black lines represent the average spindle angles. **(I)** Oscillation index in polarised and non-polarised cells, in the *xy* axis (polarised: *n* = 30 cells; non-polarised: *n* = 30 cells). Two-sided *t*-test, *P* = 0.203. **(J)** Percentage of cells with spindle oscillation in the *xy* axis (polarised: *n* = 30 cells; non-polarised: *n* = 29 cells). Two-sided *t*-test, *P* = 0.0968. All data are presented as mean ± s.e.m. from 3 or 4 independent experiments. n.s. (not significant). Source data are provided as a Source Data file.

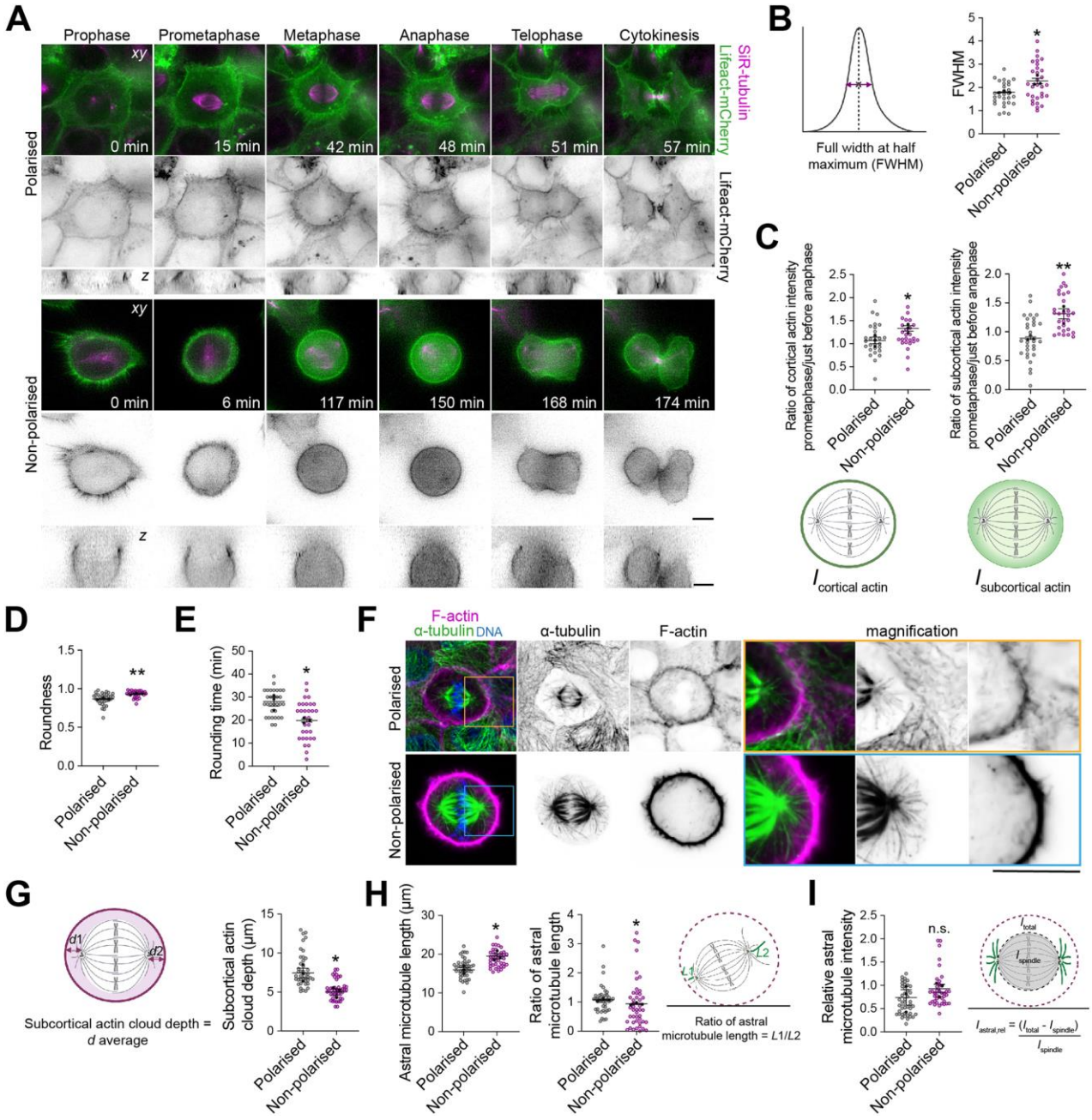

Fig. 3. Perturbation of cell-cell adhesion formation impairs F-actin and astral microtubule organisation and crosstalk. (A) Time-lapse images of representative clonal polarised and non-polarised cells MCF-10A cells stably expressing Lifeact-mCherry (green). Microtubules labelled with SiR-tubulin (magenta) 3 h before imaging. Scale bars, 10 µm. **(B)** Full width at half maximum (FWHM) for measurement of actin stiffness (polarised: *n* = 29 cells; non-polarised: *n* = 30 cells). Two-sided *t*-test, **P* = 0.0169. **(C)** Ratio of fluorescence intensity of cortical (left) and subcortical (right) actin between prometaphase and last frame of metaphase: cortical (polarised: *n* = 30 cells; non-polarised: *n* = 29 cells); subcortical (polarised: *n* = 28 cells; non-polarised: *n* = 25 cells). Two-sided *t*-test, cortical **P* = 0.044; subcortical ***P* = 0.010. **(D)** Roundness of metaphase cells (polarised: *n* = 33 cells; non-polarised: *n* = 29 cells). Two-sided *t*-test, ***P* = 0.0035. **(E)** Rounding time for polarised and non-polarised cells (polarised: *n* = 31 cells; non-polarised: *n* = 31 cells).

Two-sided *t*-test, **P* = 0.0159. **(F)** Confocal images of representative polarised and non-polarised cells stained for F-actin (magenta) and α-tubulin (green); and counterstained with Hoechst 33342 (DNA, blue). Scale bar, 10 µm. **(G)** Average subcortical actin cloud depth (*d*) in polarised and non-polarised cells (polarised: *n* = 41 cells; non-polarised: *n* = 43 cells). Two-sided *t*-test, **P* = 0.029. *d*1 and *d*2 were measured as described on the illustration. **(H)** Left: Astral microtubule length (polarised: *n* = 42 cells; non-polarised: *n* = 39 cells); right: ratio of astral microtubule length (*L*) (polarised: *n* = 42 cells; non-polarised: *n* = 45 cells). Two-sided *t*-test, astral microtubule length: **P* = 0172; ratio of astral microtubule length: **P* = 0176. *L*1 and *L*2 were measured as described on the illustration. **(I)** Relative (rel) fluorescence intensities of astral microtubules ($I_{astral, rel}$) in polarised and non-polarised cells (polarised: *n* = 43 cells; non-polarised: *n* = 39 cells). Two-sided *t*-test, *P* = 0.37. I_{total} and $I_{spindle}$ were measured as described on the illustration. All data are presented as mean ± s.e.m. from 3 or 4 independent experiments. n.s. (not significant). Source data are provided as a Source Data file.

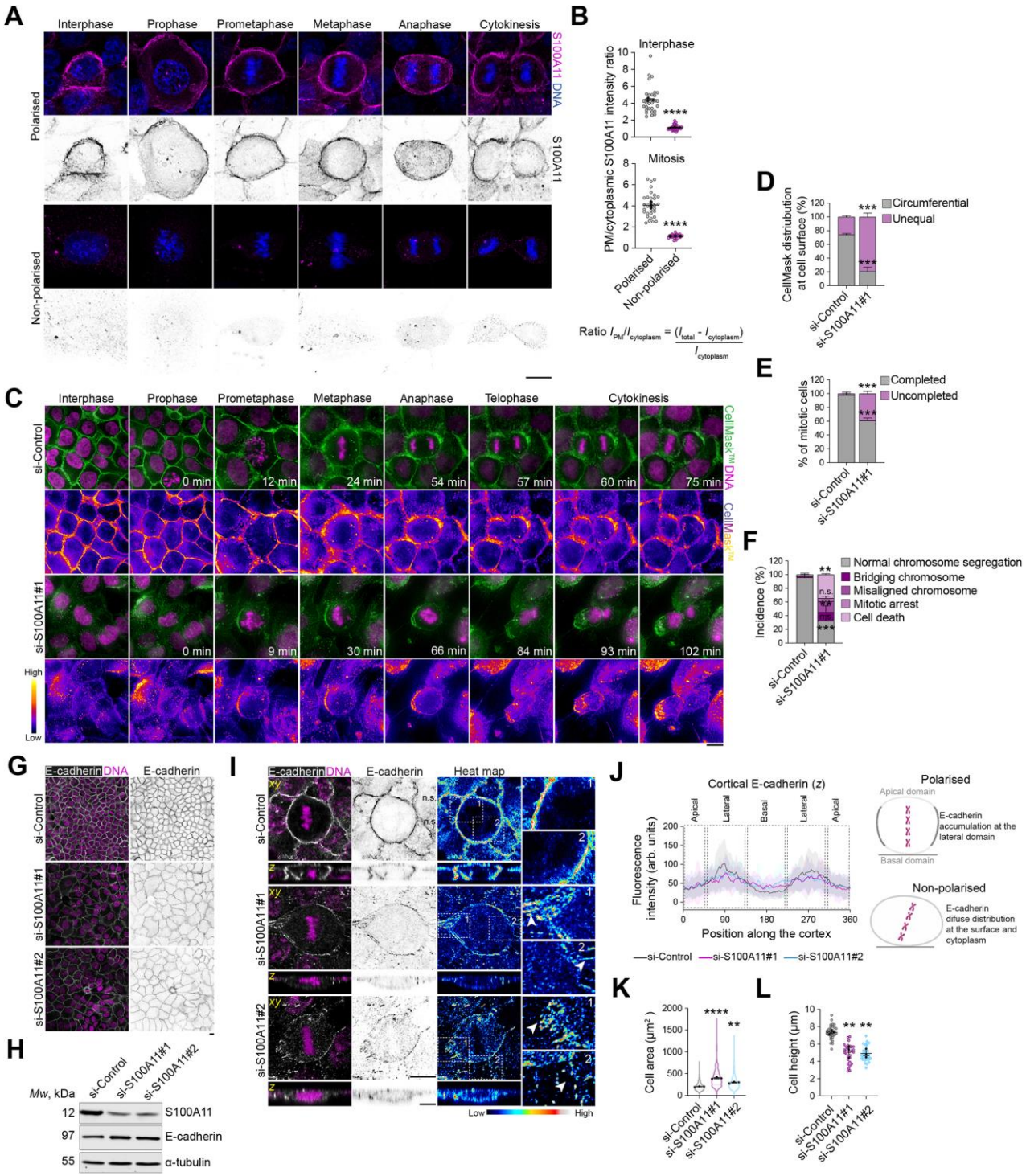

Fig. 4. S100A11 is required for correct plasma membrane remodelling and cell-cell adhesion integrity during mitosis. (A) Confocal images of representative polarised and non-polarised MCF-10A cells stained for S100A11 (magenta) and counterstained with Hoechst 33342 (DNA, blue). Scale bar, 10 µm. **(B)** Plasma membrane (PM)-to-cytoplasmic S100A11 intensity ratio in interphase and mitotic cells (polarised: *n* = 30 cells; non-polarised: *n* = 30 cells). Two-sided *t*-test, interphase: ****P < 0.0001; mitosis: ****P < 0.0001. **(C)** Time-lapse images of representative si-Control- or si-S100A11#1-treated MCF-10A cells, labelled with CellMask™ (plasma membrane, green) and Hoechst 33342 (DNA, Magenta), 10 min and 30 min before

acquisition, respectively. Scale bar, 10 µm. **(D)** Percentage of CellMask^{TM} labelling distribution at the cell surface during metaphase in siRNA-transfected cells (si-Control: *n* = 28 cells; si-S100A11#1: *n* = 59 cells). Two-sided *t*-test, Circumferential: ***P = 0.0008; Unequal: ***P = 0.0008. **(E)** Incidence of completed and uncompleted mitosis in siRNA-transfected cells (si-Control: *n* = 28 cells; si-S100A11#1: *n* = 59 cells). Two-sided *t*-test, ***P = 0.0007. **(F)** Percentage of mitotic defects in siRNA-transfected cells (si-Control: *n* = 28 cells; si-S100A11#1: *n* = 59 cells). Two-sided *t*-test, normal chromosome segregation: ***P = 0.0002; misaligned chromosome: **P = 0.0012; bridging chromosome: P = 0.308; mitotic arrest: P = 0.172; cell death: **P = 0.002. **(G)** Confocal images of representative si-Control-, si-S100A11#1, si-S100A11#2-treated cells, stained for E-cadherin (grey) and counterstained with Hoechst 33342 (DNA, magenta). Scale bar, 10 µm. **(H)** Western blotting of extracts from siRNA-transfected cells. Blots are stained for S100A11 and E-cadherin, and α-tubulin as a loading control. **(I)** Confocal images of representative si-Control-, si-S100A11#1, si-S100A11#2-treated metaphase cells stained for E-cadherin (grey) and counterstained with Hoechst 33342 (DNA, magenta). Scale bars, 10 µm. **(J)** Average cortical fluorescence intensity profiles of E-cadherin in siRNA-transfected metaphase cells (si-Control: n = 30; si-S100A11#1: n = 30; si-S100A11#2: n = 27). **(K)** Cell area in siRNA-transfected cells (si-Control: *n* = 1699 cells; si-S100A11#1: *n* = 634 cells; si-S100A11#2: *n* = 1110 cells). One-way ANOVA with Dunnett's test, ****P < 0.0001, **P = 0.002. **(L)** Cell height in siRNA-transfected cells (si-Control: *n* = 30 cells; si-S100A11#1: *n* = 30 cells; si-S100A11#2: *n* = 29 cells). One-way ANOVA with Dunnett's test, **P = 0.0032, **P = 0.0019. All data are presented as mean ± s.e.m. from 3 or 4 independent experiments. n.s. (not significant). Source data are provided as a Source Data file.

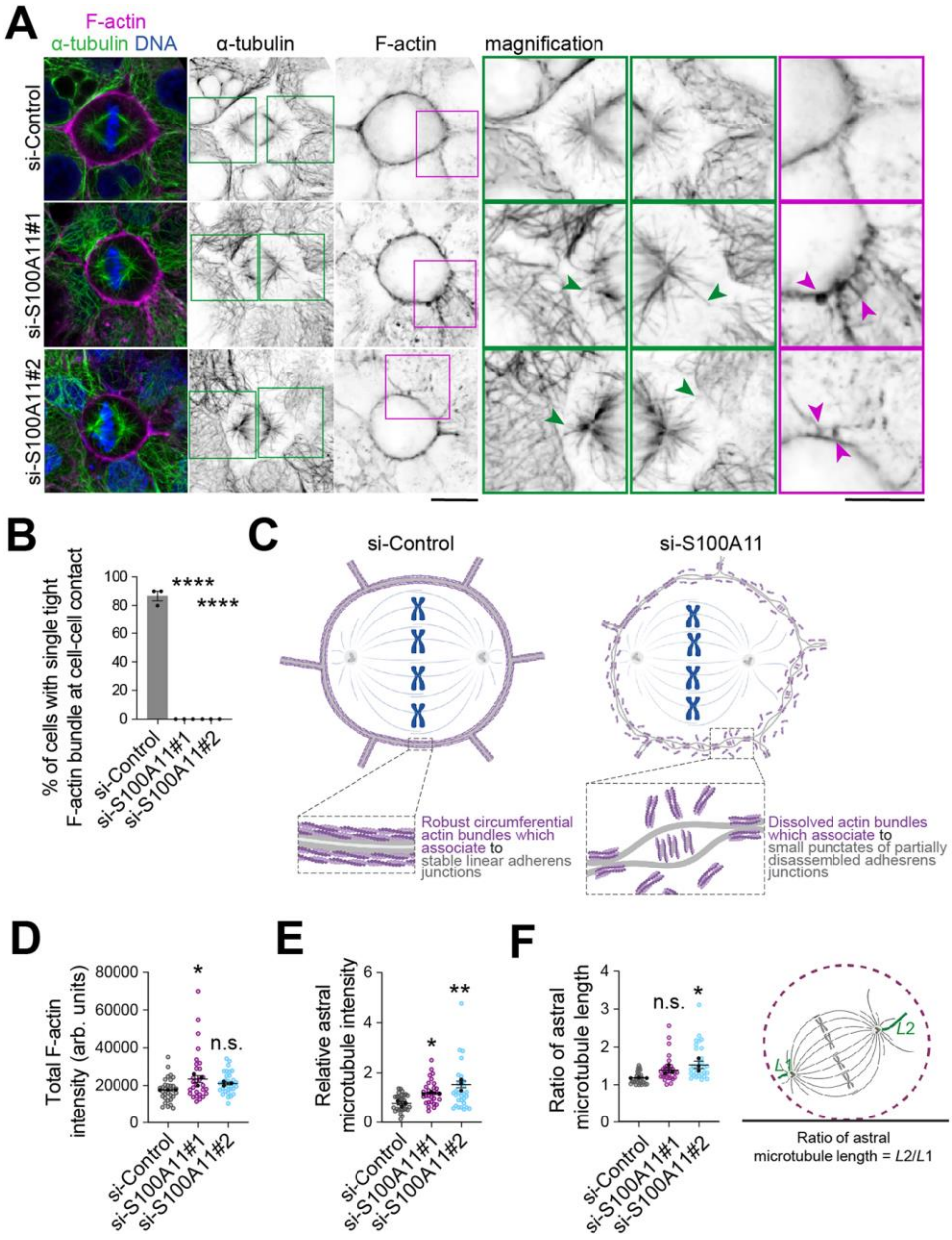

Fig. 5. S100A11 is required for F-actin and astral microtubule organisation during mitosis. **(A)** Confocal images of representative si-Control-, si-S100A11#1-, si-S100A11#2-treated metaphase cells stained for α-tubulin (green) and F-actin (magenta), and counterstained with Hoechst 33342 (DNA, blue). Scale bars, 10 µm. **(B)** Percentage of cells with single tight F-actin bundle formation at cell-cell contact in siRNA-transfected cells (si-Control: *n* = 30 cells; si-S100A11#1: *n* = 36 cells; si-S100A11#2: *n* = 38 cells). One-way ANOVA with Dunnett's test, ****P < 0.0001; ****P < 0.0001. **(C)** Illustration showing F-actin bundles at cell-cell contacts and the effect of S100A11 knockdown on their assembly. **(D)** Fluorescence intensity of total actin in siRNA-transfected cells (si-Control: *n* = 32 cells; si-S100A11#1: *n* = 29 cells; si-S100A11#2: *n* = 31 cells). One-way ANOVA with Dunnett's test, *P = 0.019; P = 0.185. **(E)** Relative fluorescence intensity of astral microtubules in siRNA-transfected cells (si-Control: *n* = 31 cells; si-S100A11#1:

n = 30 cells; si-S100A11#2: *n* = 30 cells). One-way ANOVA with Dunnett's test, **P* = 0.0251 and ***P* = 0.0015. **(F)** Ratio of astral microtubule length in siRNA-transfected cells (si-Control: *n* = 29 cells; si-S100A11#1: *n* = 29 cells; si-S100A11#2: *n* = 29 cells). One-way ANOVA with Dunnett's test, *P* = 0.130; **P* = 0.021. All data are presented as mean ± s.e.m. from 3 or 4 independent experiments. n.s. (not significant). Source data are provided as a Source Data file.

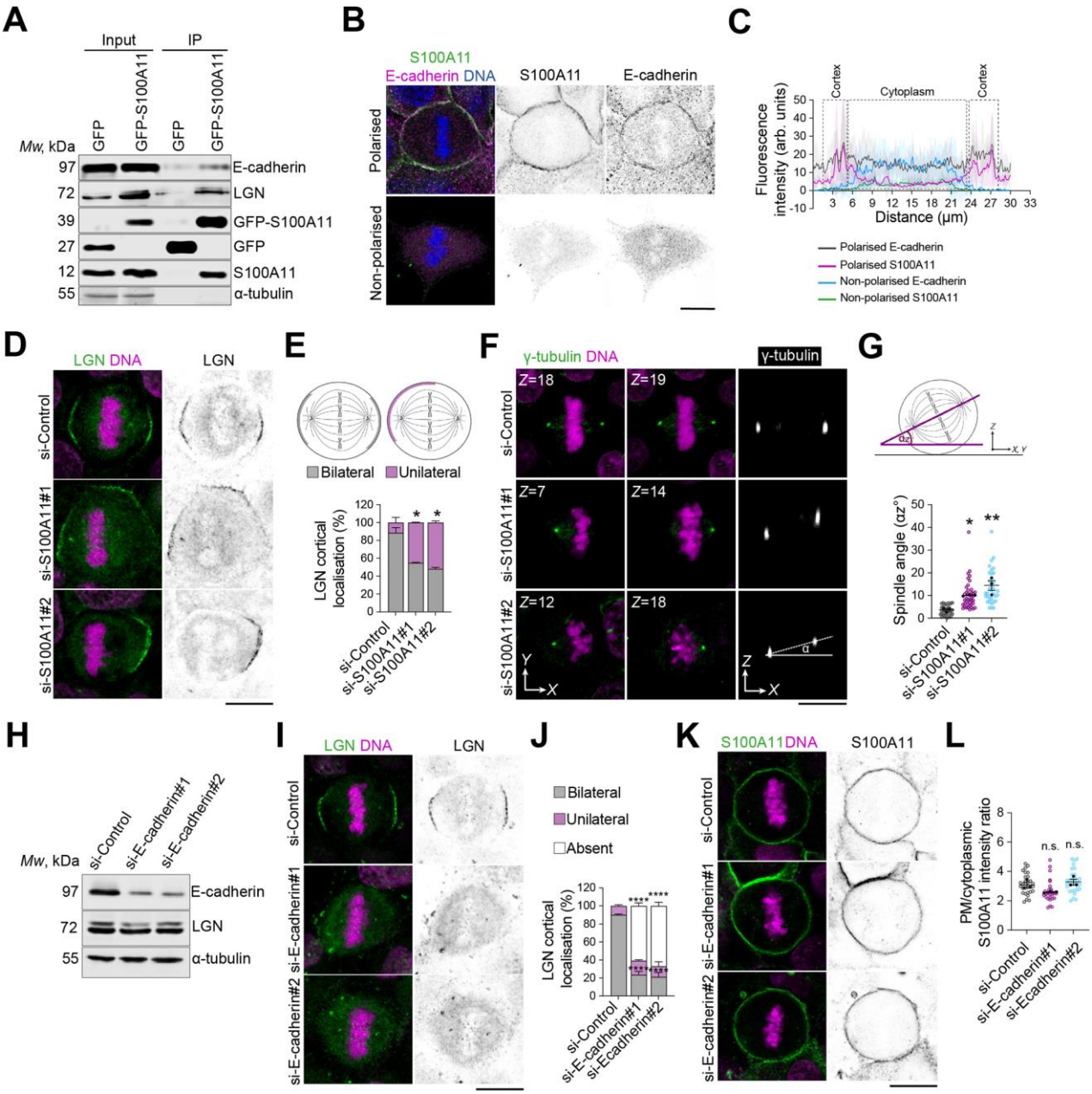

Fig. 6. S100A11 complexes with E-cadherin and LGN to regulate E-cadherin-LGN mediated mitotic spindle orientation. (A) GFP-S100A11, E-cadherin and LGN co-immunoprecipitates from clonal MCF-10A stably expressing GFP-S100A11, arrested in metaphase. Lysates were subjected to affinity purification with GFP-Trap beads. The immunoprecipitates (IP) were analysed by western blotting. **(B)** Confocal images of representative polarised and non-polarised MCF-10A cells stained for S100A11 (green) and E-cadherin (magenta); and counterstained with Hoechst 33342 (DNA, blue). Scale bar, 10 µm. **(C)** Average cortical and cytoplasmic relative fluorescence intensity profiles of E-cadherin and S100A11 in 10 representative polarised cells and 10 representative non-polarised cells, during metaphase. **(D)** Confocal images of representative si-Control-, si-S100A11#1- and si-S100A11#2-treated metaphase cells stained for LGN (green) and counterstained with Hoechst 33342 (DNA, magenta). Scale bar, 10 µm. **(E)** Percentage of cortical localisation of LGN in siRNA-transfected cells (si-Control: *n* = 64 cells; si-

S100A11#1: *n* = 64 cells; si-S100A11#2: *n* = 49 cells). Two-way ANOVA with Tukey's test, **P* = 0.016; **P* = 0.0104; *P* = 0.924, respectively. **(F)** Confocal images of representative si-Control-, si-S100A11#1, si-S100A11#2-treated metaphase cells stained for γ-tubulin (green) and counterstained with Hoechst 33342 (DNA, magenta). Scale bar, 10 µm. **(G)** Mitotic spindle angle α*z* in siRNA-transfected metaphase cells (si-Control: *n* = 37 cells; si-S100A11#1: *n* = 41 cells; si-S100A11#2: *n* = 36 cells). One-way ANOVA with Dunnett's test, **P* = 0.025; ***P* = 0.002, respectively. **(H)** Western blotting of extracts from siRNA-transfected cells. Blots are stained with E-cadherin, LGN and α-tubulin as a loading control. **(I)** Confocal images of representative si-Control-, si-E-cadherin#1, si-E-cadherin#2-treated metaphase cells stained for LGN (green) and counterstained with Hoechst 33342 (DNA, magenta). Scale bars, 10 µm. **(J)** Percentage of cortical localisation of LGN in siRNA-transfected cells (si-Control: *n* = 39 cells; si-E-cadherin#1: *n* = 51 cells; si-E-cadherin #2: *n* = 43 cells). Two-way ANOVA with Dunnett's test, Bilateral: *****P* <0.0001 and *****P* <0.0001; Unilateral: *P* = 0.379 and *P* = 0.891; Absent: *****P* < 0.0001 and *****P* <0.0001. **(K)** Confocal images of representative si-Control-, si-E-cadherin#1-, si-E-cadherin#2-treated metaphase cells stained for S100A11 (green) and counterstained with Hoechst 33342 (DNA, magenta). Scale bars, 10 µm. **(L)** plasma membrane (PM)-to-cytoplasmic ratio of S100A11 fluorescence intensities in siRNA-transfected cells (si-Control: *n* = 30 cells; si-E-cadherin#1: *n* = 30 cells; si-E-cadherin #2: *n* = 30 cells). One-way ANOVA with Dunnett's test, *P* = 0.114; *P* = 0.589. All data are presented as mean ± s.e.m. from 2, 3 or 4 independent experiments. n.s. (not significant). Source data are provided as a Source Data file.

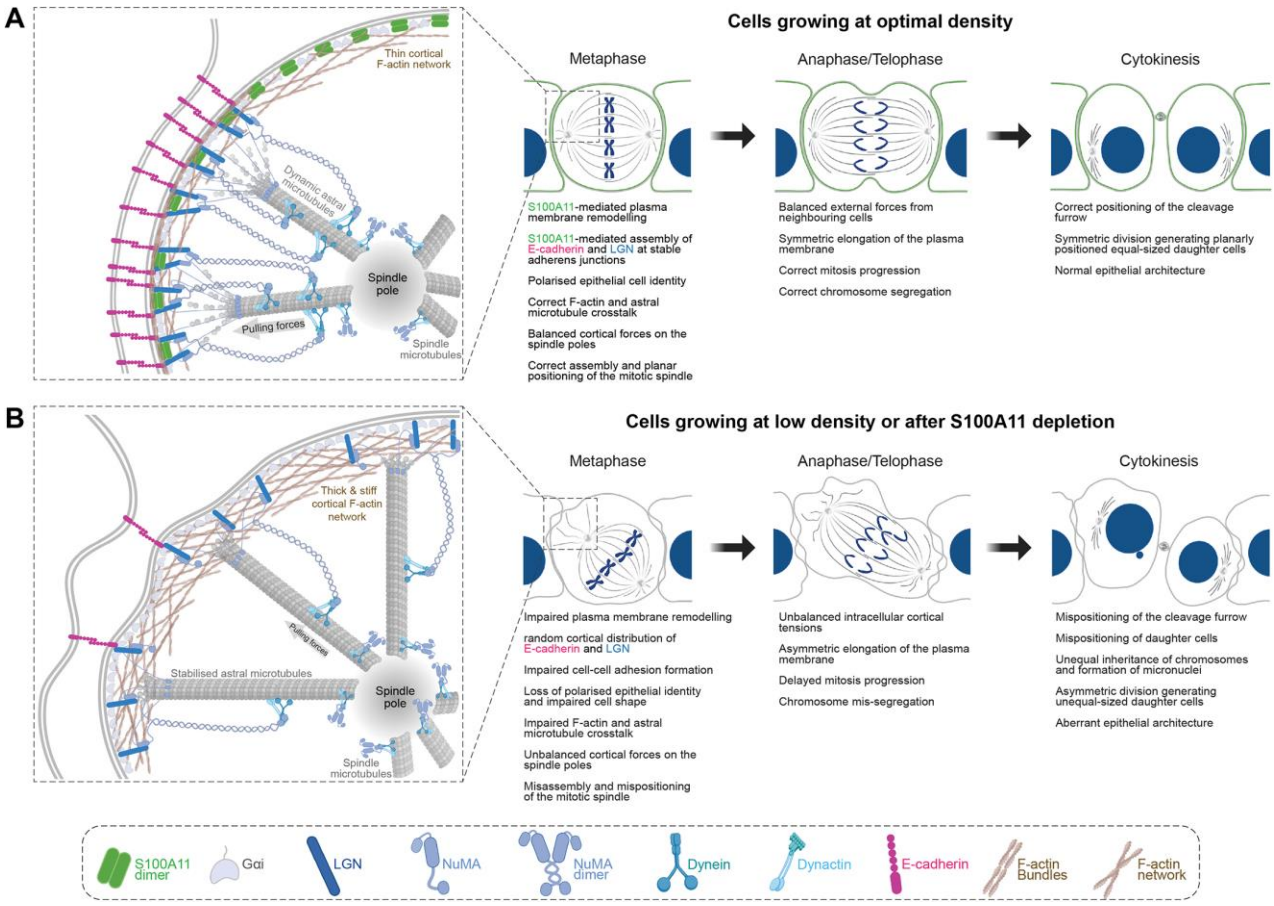

Fig. 7. Proposed model for the role of S100A11-mediated plasma membrane remodelling in the regulation of polarised epithelial cell divisions. (A) S100A11 associates to the plasma membrane of polarised mammary epithelial cells grown at optimal density to regulate its remodelling during metaphase, which in turn controls mitotic cell shape. This along with the formation of a complex between S100A11, E-cadherin and LGN ensures correct organisation of the cortex and polarised accumulation of E-cadherin and LGN at the lateral cortex, thereby maintaining epithelial cell identity and ensuring proper LGN-mediated mitotic spindle assembly and orientation. Consequently, cells execute and achieve correct polarised divisions. **(B)** In cells grown at low density or at optimal density after S100A11 depletion, S100A11 is lost at the plasma membrane which undergoes aberrant remodelling, impairing mitotic cell shape. This also impairs the localisation of E-cadherin and LGN at the cell cortex, which is thicker and stiffer. In these conditions cells lose their epithelial identity and fail to properly assemble and orient their mitotic spindle during metaphase. Subsequently, this results in aberrant mitosis mechanics, progression, and outcome.

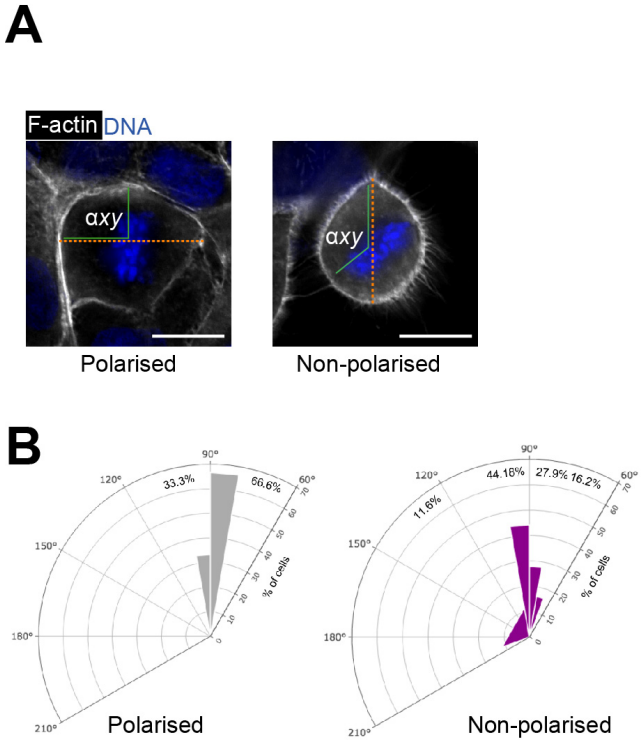

Fig. S1. The mitotic spindle aligns following Hertwig's rule in polarised cells but not in non-polarised cells. (A) Confocal images of representative polarised and non-polarised MCF-10A cells stained for F-actin (grey) and counterstained with Hoechst 33342 (DNA, blue). The orange dashed line indicates the long axis of the cell. The angle α*xy* indicates the orientation of the metaphase plate relative to the long axis of the cell. Scale bar, 10 µm. **(B)** α*xy* angle frequencies in polarised and non-polarised cells (polarised: *n* = 45 cells; non-polarised: *n* = 40 cells, 3 independent experiments).

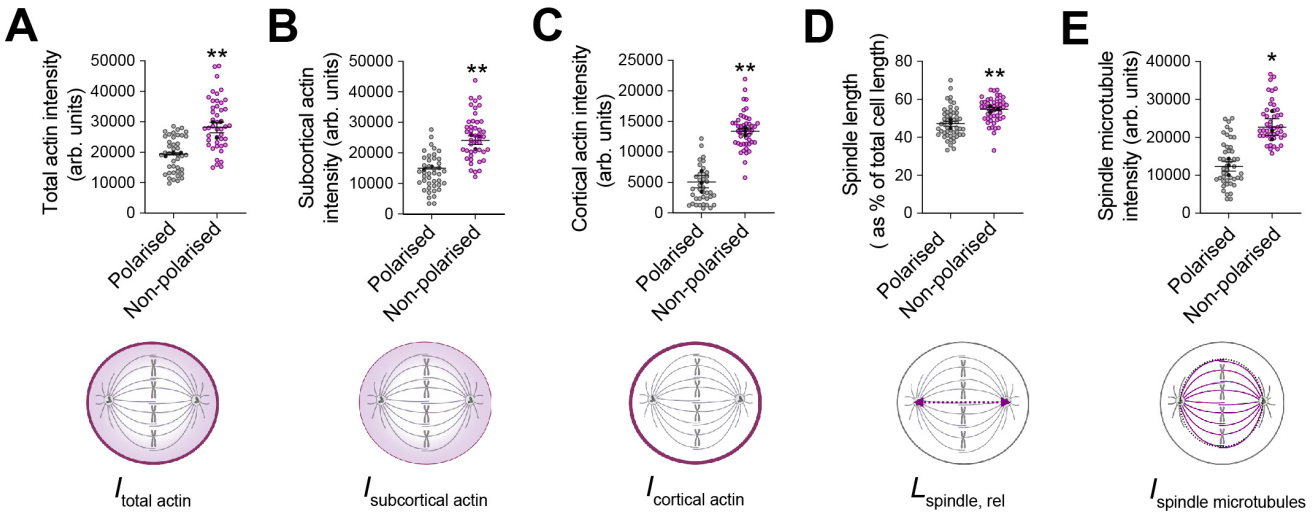

Fig. S2. Perturbation of cell-cell adhesion formation affects F-actin organisation and mitotic spindle assembly in fixed metaphase cells. (A-C) Fluorescence intensity of total F-actin, subcortical F-actin, and cortical F-actin in polarised and non-polarised MCF-10A cells (polarised: n = 42 cells; non-polarised: n = 45 cells). Two-sided t-test, total: $^{**}P$ = 0.0082; subcortical: $^{**}P$ = 0.0035; cortical: $^{**}P$ = 0.0015. **(D)** Spindle length in metaphase (polarised: n = 51 cells; non-polarised: n = 47 cells). Two-sided t-test, $^{**}P < 0.0094$. **(E)** Relative fluorescence intensity of spindle microtubules (polarised: n = 46 cells; non-polarised: n = 44 cells). Two-sided t-test, $^{*}P$ = 0.0147. All data are presented as mean ± s.e.m. from 3 or 4 independent experiments. Source data are provided as a Source Data file.

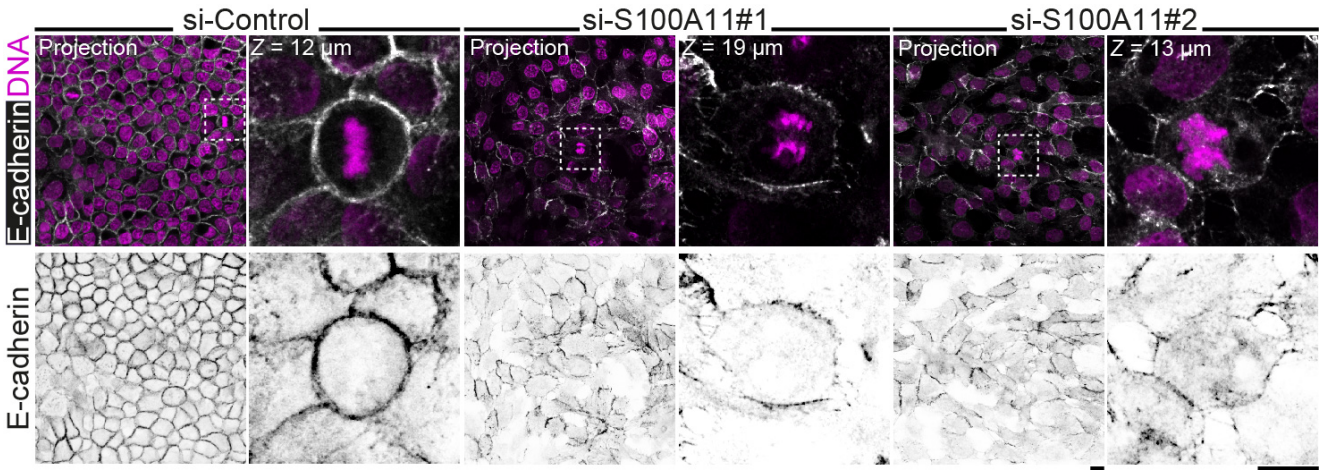

Fig. S3. Defects in cell-cell adhesion persist at 72 h post-S100A11 knockdown. Confocal images of representative si-Control-, si-S100A11#1, si-S100A11#2-treated cells stained for E-cadherin (grey) and counterstained with Hoechst 33342 (DNA, magenta). Scale bar, 10 µm.

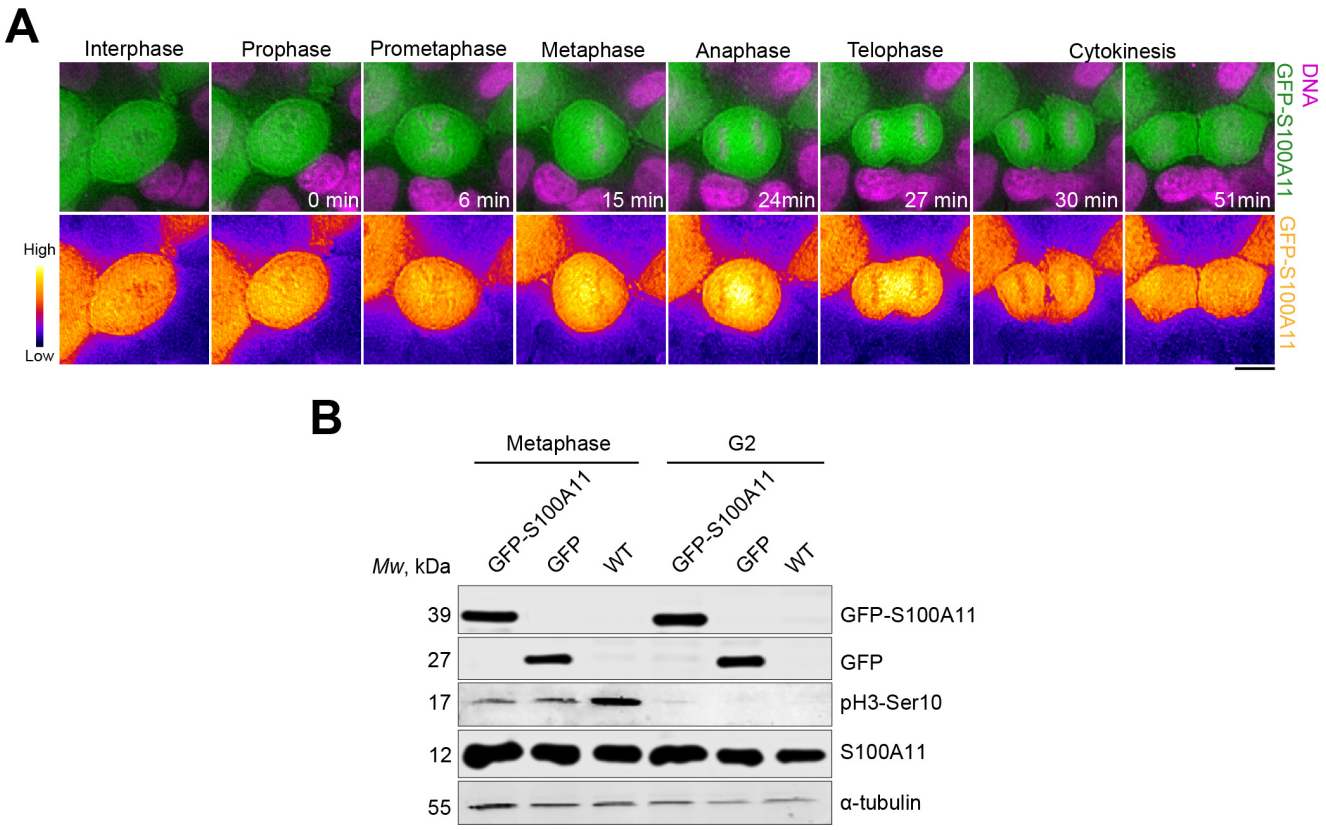

Fig. S4. Validation of the cell-cycle synchronisation protocol in mammary epithelial cells. (A) Time-lapse images of representative clonal MCF-10A cells stably expressing GFP-S100A11 (green). DNA is labelled with Hoechst 33342 (magenta). Scale bar, 10 µm. **(B)** Western blotting of extracts from wild type MCF-10A and clonal MCF-10A stably expressing GFP-S100A11 or GFP cells, synchronised in G2 or metaphase. Blots are stained for GFP, S100A11 and phospho-histone H3 (pH3-ser10), and α-tubulin as a loading control (3 independent experiments). Source data are provided as a Source Data file.

Figure 4H

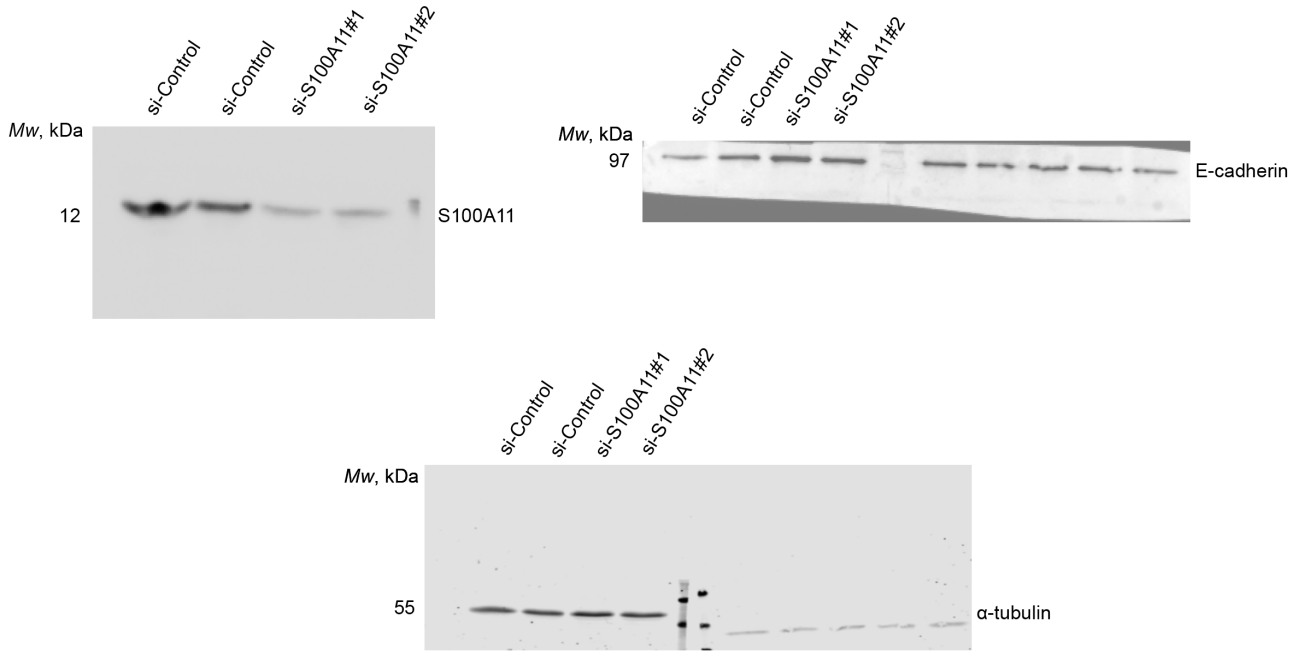

Fig. S5. Blot Transparency. Images of the uncropped blots with molecular weight markers (in kDa) are shown for all corresponding figures and supplementary figures.

Figure 6A

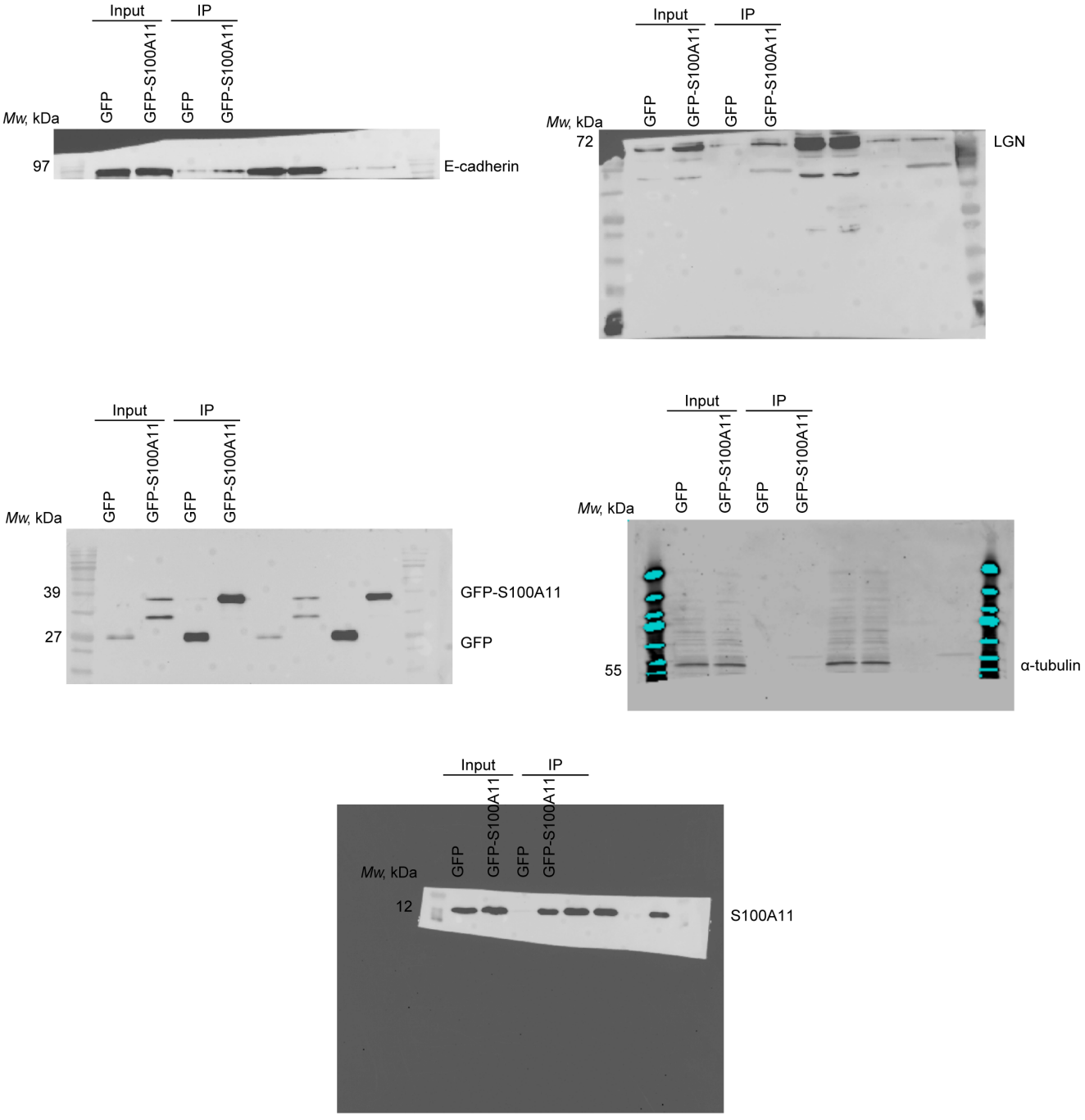

Figure 6H

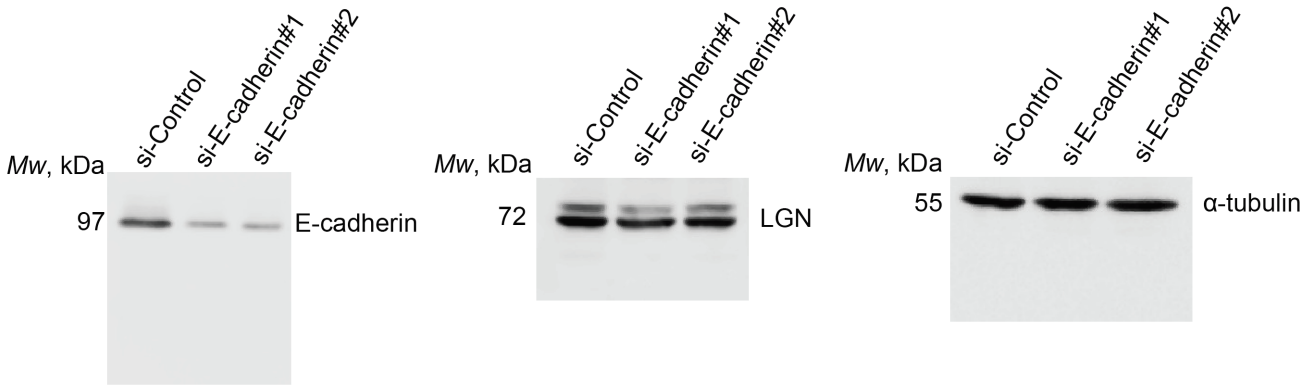

Figure S4B

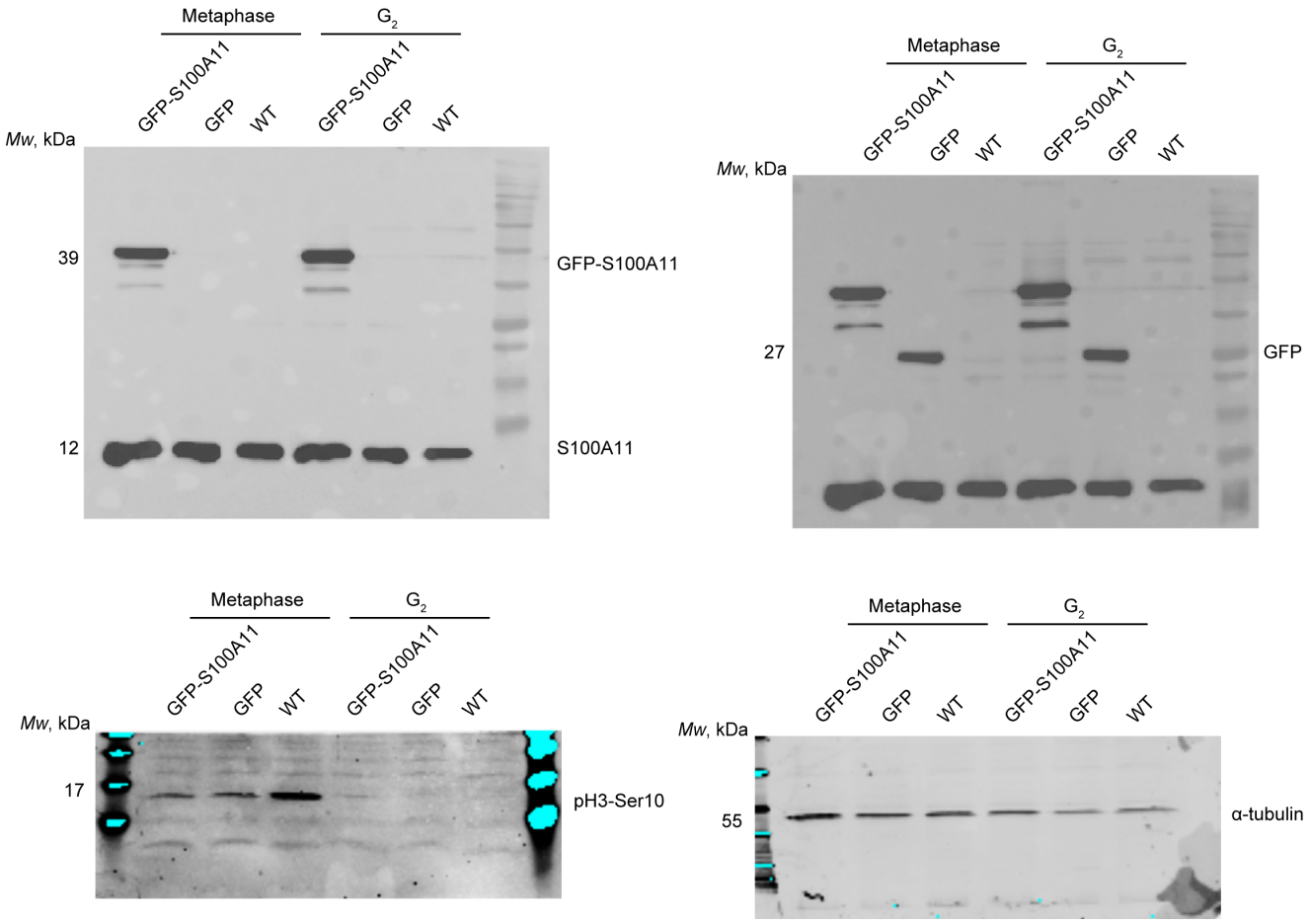

Table S1.

Available for download at
https://journals.biologists.com/jcs/article-lookup/doi/10.1242/jcs.261701#supplementary-data

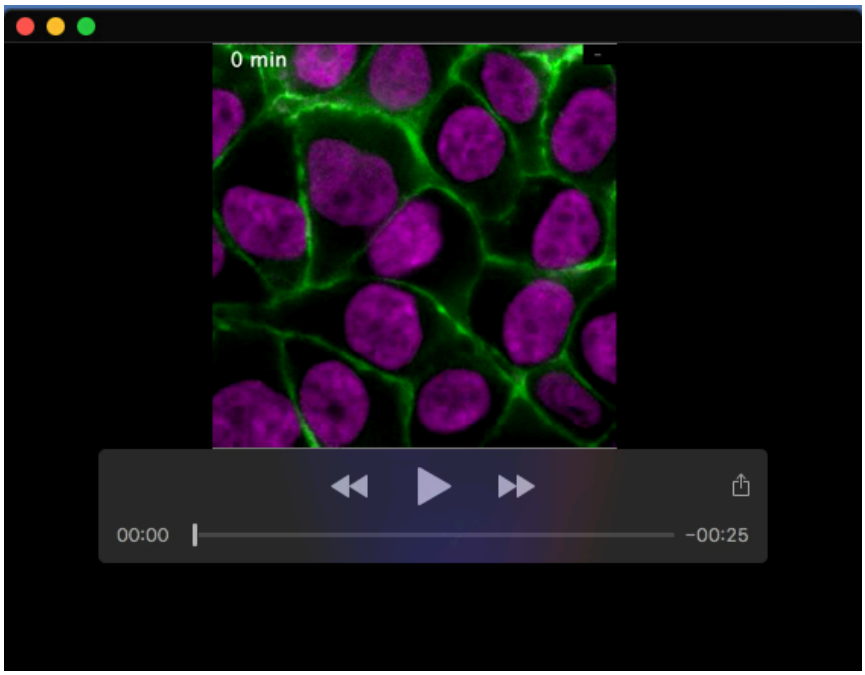

Movie 1. Description: CellMask™ circumferential distribution at the plasma membrane and correct mitosis dynamic progression and outcome in polarised MCF-10A cells. Maximum intensity projections of CellMask™ (green) and Hoechst (DNA, magenta) are shown through time (min).

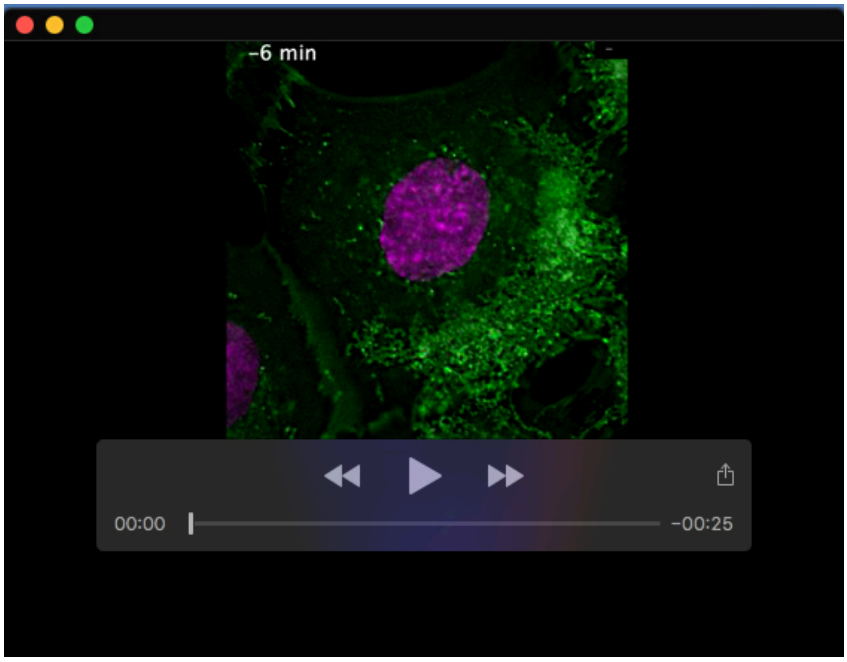

Movie 2. Description: Perturbation of cell-cell adhesion formation results in unilateral distribution of CellMask™ and asymmetric elongation of the plasma membrane and impairs mitosis dynamic progression and generates unequal-sized daughter cells in non-polarised MCF-10A cells. Maximum intensity projections of CellMask™ (green) and Hoechst (DNA, magenta) are shown through time (min).

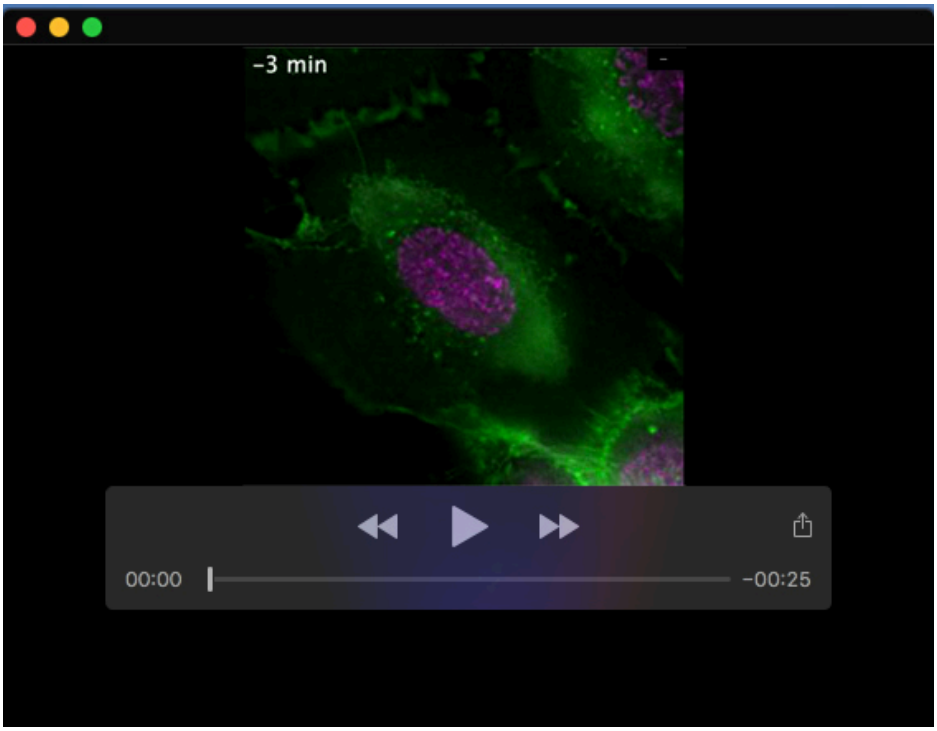

Movie 3. Description: Perturbation of cell-cell adhesion formation results in bilateral distribution of CellMask™ and at the plasma membrane and delayed mitosis progression in non-polarised MCF-10A cells. Maximum intensity projections of CellMask™ (green) and Hoechst (DNA, magenta) are shown through time (min).

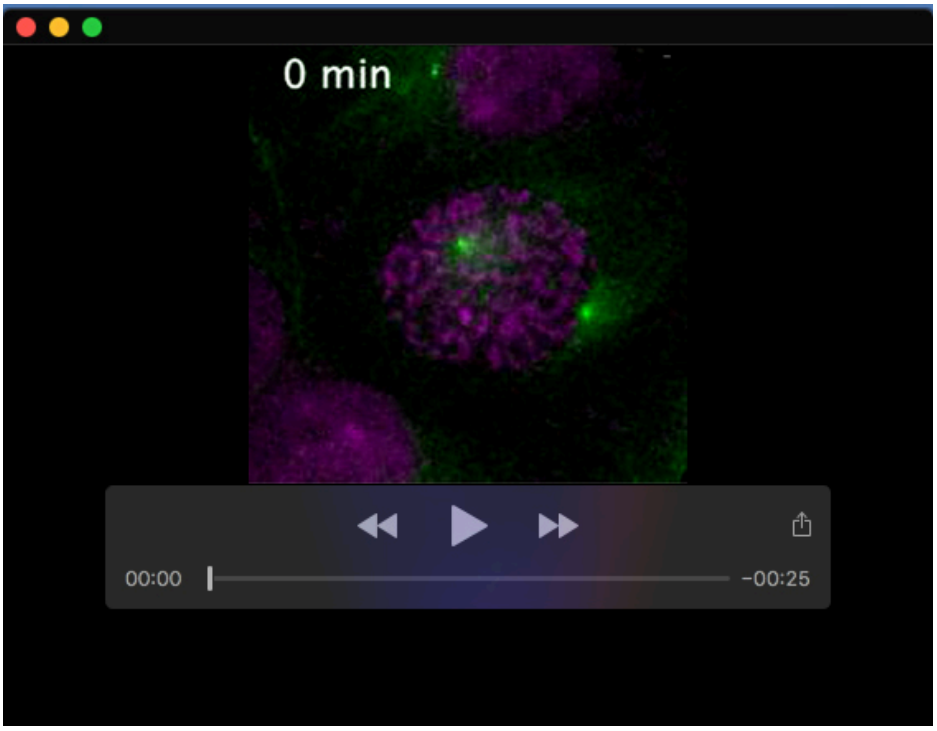

Movie 4. Description: Correct mitotic spindle and chromosome dynamics and mitosis progression and outcome in polarised MCF-10A cells. Maximum intensity projections of SiR-tubulin (green) and Hoechst (DNA, magenta) are shown through time (min).

Journal of Cell Science • Supplementary information

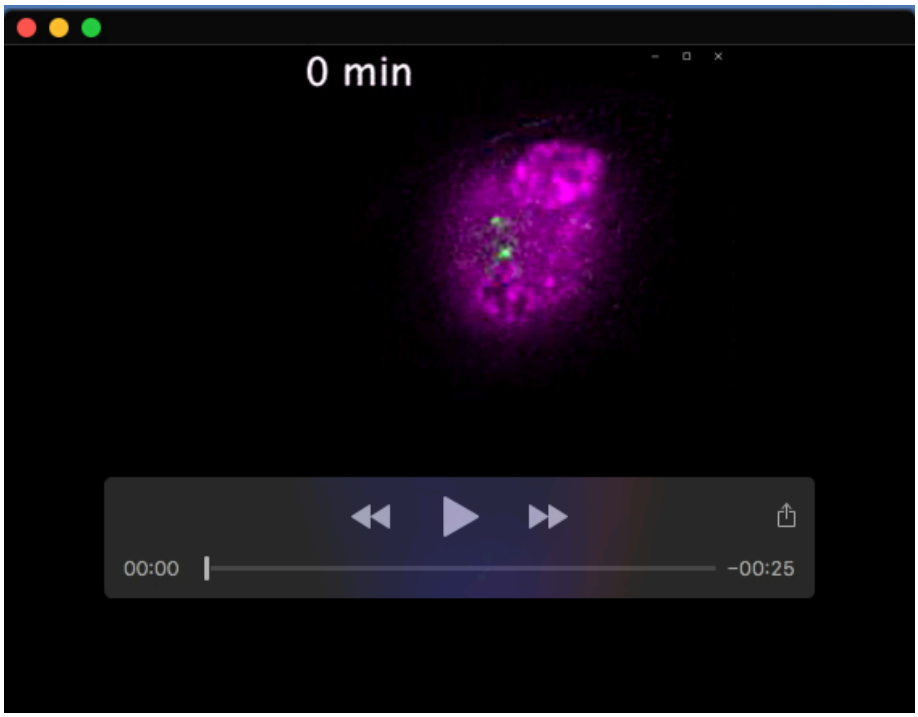

Movie 5. Description: Perturbation of cell-cell adhesion formation results in chromosome mis-segregation, micronuclei, and delayed mitosis progression in non-polarised MCF-10A cells. Maximum intensity projections of SiR-tubulin (green) and Hoechst (DNA, magenta) are shown through time (min).

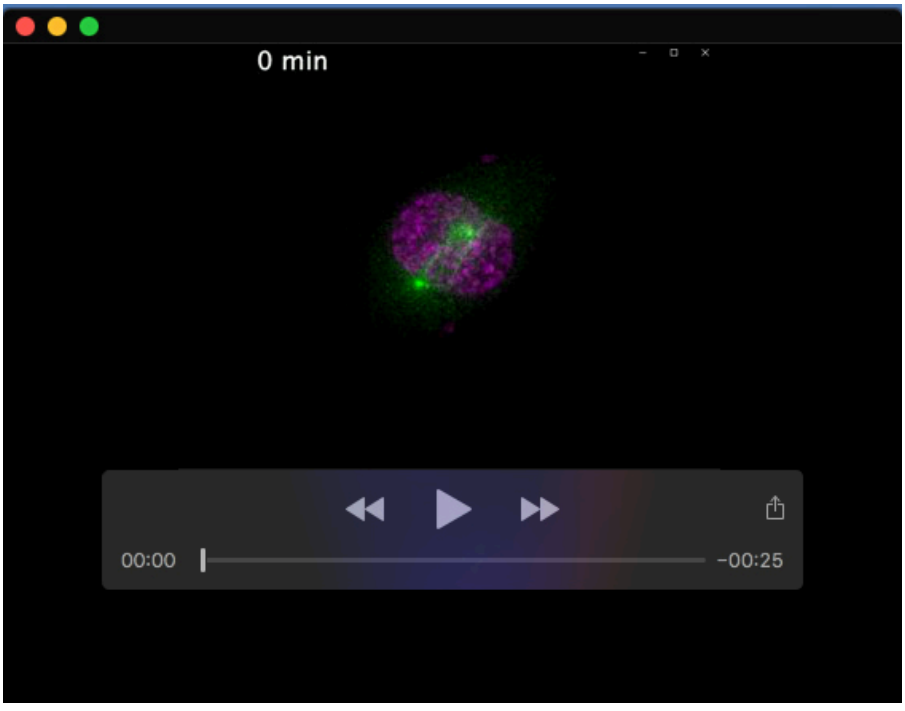

Movie 6. Description: Perturbation of cell-cell adhesion formation results in chromosome bridges and delayed mitosis progression in non-polarised MCF-10A cells. Maximum intensity projections of SiR-tubulin (green) and Hoechst (DNA, magenta) are shown through time (min).

Journal of Cell Science • Supplementary information

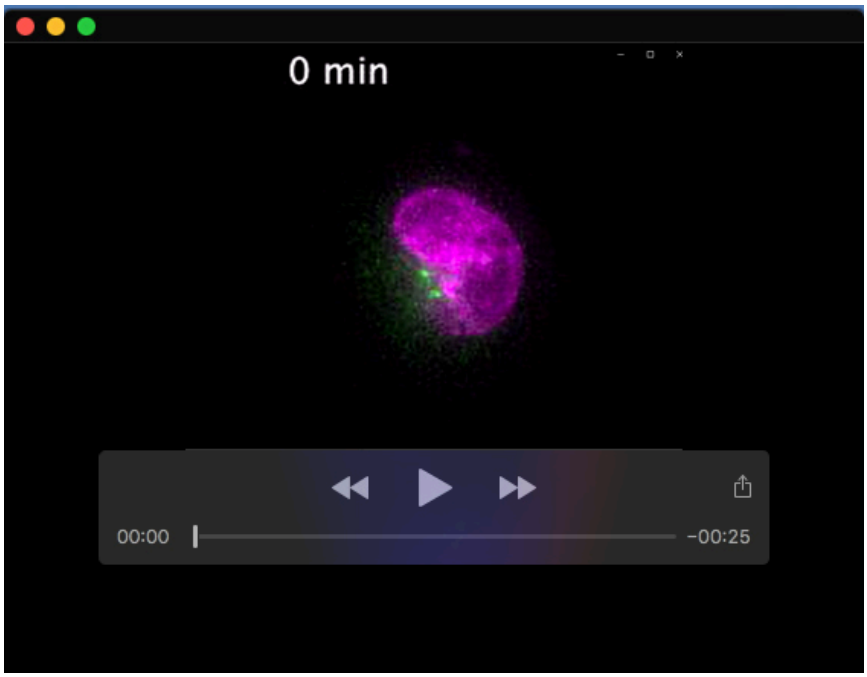

Movie 7. Description: Perturbation of cell-cell adhesion formation results in mitotic spindle dynamic and assembly defects, and mitotic arrest in non-polarised MCF-10A cells. Maximum intensity projections of SiR-tubulin (green) and Hoechst (DNA, magenta) are shown through time (min).

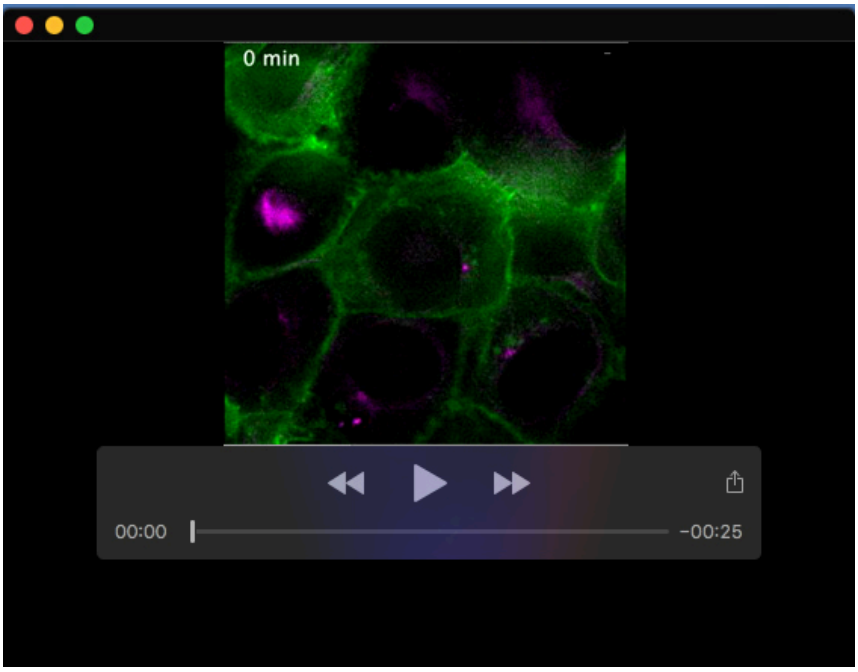

Movie 8. Description: Correct F-actin dynamic re-organisation and mitotic spindle dynamics and mitosis progression in polarised MCF-10A cells stably expressing Lifeact-mCherry. Maximum intensity projections of Lifeact-mCherry (F-actin, green) and SiR-tubulin (magenta) are shown through time (min).

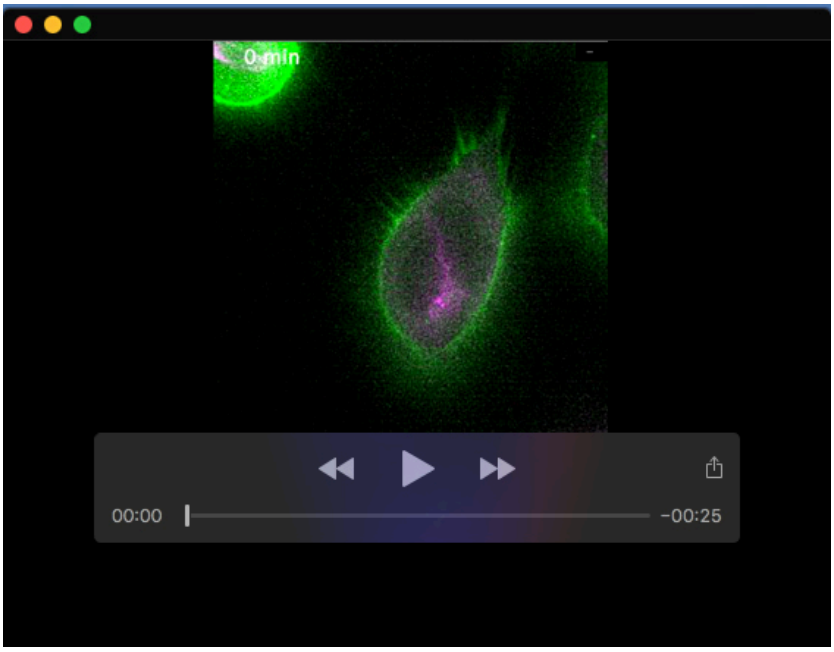

Movie 9. Description: Perturbation of cell-cell adhesion formation affects F-actin re-organisation and results in mitotic spindle assembly and dynamic defects and impairs mitosis progression and outcome in non-polarised MCF-10A cells stably expressing Lifeact-mCherry. Maximum intensity projections of Lifeact-mCherry (F-actin, green) and SiR-tubulin (magenta) are shown through time (min).

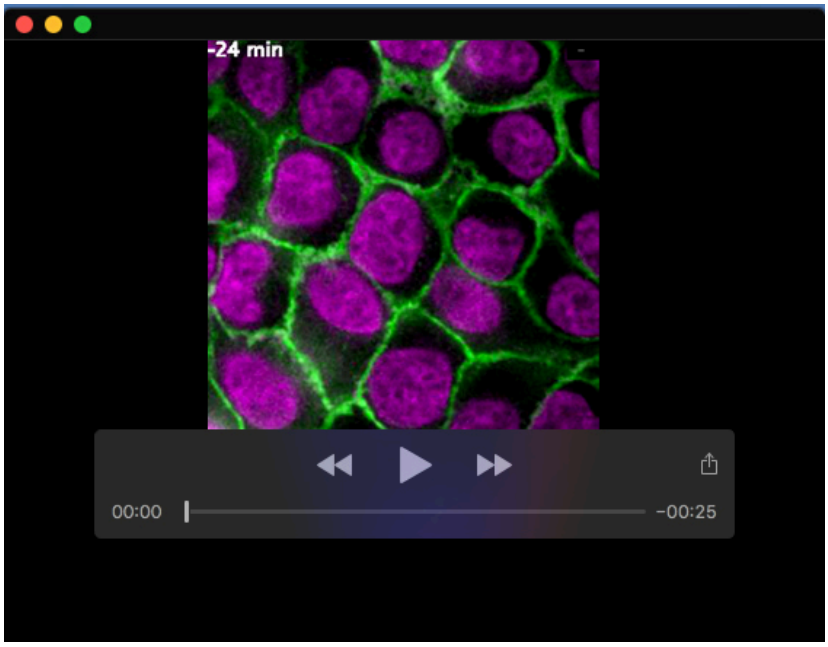

Movie 10. Description: CellMask™ circumferential distribution at the plasma membrane and correct dynamics of mitosis in polarised MCF-10A cells treated with si-Control. Maximum intensity projections of CellMask™ (green) and Hoechst (DNA, magenta) are shown through time (min).

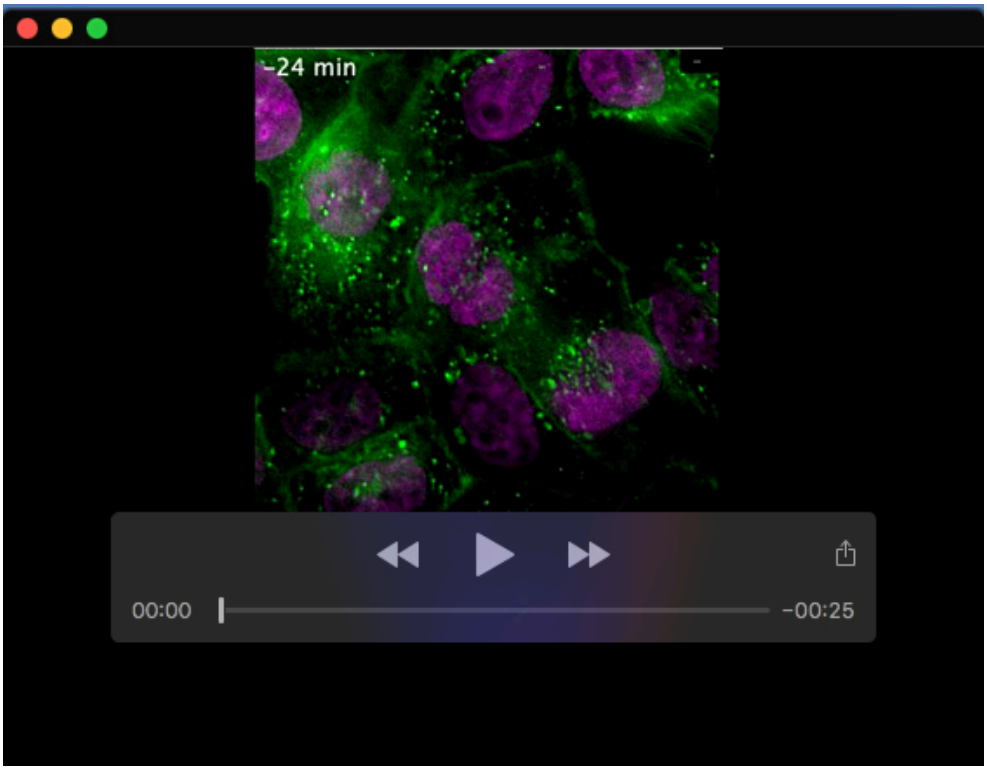

Movie 11. Description: S100A11 knockdown (si-S100A11#1) in polarised MCF-10A cells results in unilateral distribution of CellMask™ and asymmetric elongation of the plasma membrane and impairs mitosis dynamic progression and outcome. Maximum intensity projections of CellMask™ (green) and Hoechst (DNA, magenta) are shown through time (min).

Movie 12. Description: S100A11 spatiotemporal distribution in polarised MCF-10A cells stably expressing GFP-S100A11. Maximum intensity projections of GFP-S100A11 (green) and Hoechst (DNA, magenta) are shown through mitosis phases.